MATERIAL ENGINEERING MASTER THESIS

SINTERABILITY STUDY OF LUNAR AND MARTIAN REGOLITH SIMULANTS BY CONVENTIONAL AND NON-CONVENTIONAL METHODS

Author: Aurore GILBERT

Supervisors: Amparo BORELL TOMÁS
              Rut BENAVENTE MARTÍNEZ

Academic Year: 2021/2022

Sinterability study of lunar and Martian regolith simulants by conventional and non-conventional methods.

Abstract

The design and construction of a permanent base on the Moon, and on Mars in a more distant future, is one of the greatest challenges space organisms are facing today. Experts and advocates of space exploration are convinced that lunar colonization is the next logical step in human expansion. Currently, it is evident that a major disadvantage of this initiative is the transportation and handling of raw materials from Earth. The direct use of materials extracted from the lunar or Martian soil, called regoliths, as construction material and tools would greatly lower costs. Based on this premise, it is necessary to carry out an exhaustive study of these regoliths as material for use. However, another added problem is that the amount of lunar regolith brought to earth is limited, and currently, there is no Martian soil sample, for it is necessary to use simulants of these materials to continue the investigation.

The main objective of this Final Master Project is to study the sinterability of simulants of lunar regoliths [Lunar Highlands Simulant (LHS-1) and Lunar Mare Simulant (LMS-1)] and of Mars [Mars Global Simulant (MGS-1)].

The first step will be the characterization of the simulant powders. The density, thermal expansion and size distribution of the particles will be determined. Different high-energy grinding will be carried out to establish the relationship between grain size and sinterability. Subsequently, these materials will be sintered using conventional and non-conventional techniques, using single-mode and multi-mode microwaves. Different temperatures and maintenance times will be studied. As the objective is to see the effect of each parameter on the quality of the final samples obtained, the materials will be characterized by electron microscopy and mechanical tests.

Keywords: Lunar regolith, Martian regolith, sintering, microwaves, structural properties

Sinterability study of lunar and Martian regolith simulants by conventional and non-conventional methods.

Resumen

El diseño y la construcción de una base permanente en la Luna y en Marte, en un futuro algo más lejano, es uno de los mayores retos a los que se enfrentan los organismos espaciales. Los expertos y defensores de la exploración espacial están convencidos de que la colonización lunar es el siguiente paso lógico en la expansión del ser humano. En estos momentos, es evidente que una de las mayores desventajas con las que cuenta esta iniciativa, es el transporte y el manejo de materias primas desde la Tierra. El uso directo de materias extraídas del suelo lunar o marciano, llamadas *regolitos*, como material de construcción y utensilios abarataría enormemente los costes. Partiendo de esta premisa, es necesario realizar un estudio exhaustivo de estos regolitos como material de uso, sin embargo, otro problema añadido es que la cantidad de regolito lunar traído a la tierra es limitada, y actualmente, no hay muestra de suelo marciano, por ello es necesario utilizar simulantes de estos materiales para continuar la investigación.

Este Proyecto Fin de Máster, tiene como principal objetivo el estudio de la sinterabilidad de simulantes de regolitos lunares [*Lunar Highlands Simulant* (LHS-1) y *Lunar Mare Simulant* (LMS-1)] y de Marte [*Mars Global Simulant* (MSG-1)].

El primer paso será la caracterización de los polvos de simulante. Se determinará la densidad, la dilatación térmica y la distribución del tamaño de las partículas. Se realizarán distintas moliendas de alta energía para establecer la relación entre tamaño de grano y la sinterizabilidad. Posteriormente, estos materiales se sinterizarán mediante técnicas convencionales y no-convencionales, mediante microondas mono-modo y multi-modo. Se estudiarán diferentes temperaturas, y tiempos de mantenimiento. Como el objetivo es ver el efecto de cada parámetro en la calidad de las muestras finales obtenidas, se caracterizarán los materiales mediante microscopía electrónica y ensayos mecánicos.

Palabras clave: Regolito lunar, regolito marciano, sinterización, microondas, propiedades estructurales.

Sinterability study of lunar and Martian regolith simulants by conventional and non-conventional methods.

Resum

El disseny i la construcció d'una base permanent en la Lluna i en Mart, en un futur una mica més llunyà, és un dels majors reptes als quals s'enfronten els organismes espacials. Els experts i defensors de l'exploració espacial estan convençuts que la colonització llunar és el següent pas lògic en l'expansió de l'ésser humà. En aquests moments, és evident que un dels majors desavantatges amb les quals compta aquesta iniciativa, és el transport i el maneig de matèries primeres des de la Terra. L'ús directe de matèries extretes del sòl llunar o sòl de marcià, anomenades *regolitos*, com a material de construcció i utensilis abarataria enormement els costos. Partint d'aquesta premissa, és necessari realitzar un estudi exhaustiu d'aquests regolitos com a material d'ús, no obstant això, un altre problema afegit és que la quantitat de regolito llunar portat a la terra és limitada, i actualment, no hi ha mostra de sòl marcià, per això és necessari utilitzar simulants d'aquests materials per a continuar la investigació.

Aquest Projecte Fi de Màster, té com a principal objectiu l'estudi de la sinterabilitat de simulants de regolitos llunars [*Highlands Simulant* (LHS-1) i *Lunar Mare Simulant* (LMS-1)] i de Mart [*Mars Global Simulant* (MSG-1)].

El primer pas serà la caracterització de les pólvores de simulant. Es determinarà la densitat, la dilatació tèrmica i la distribució de la grandària de les partícules. Es realitzaran diferents moltaes d'alta energia per a establir la relació entre grandària de gra i la sinterizabilitat. Posteriorment, aquests materials es sinteritzaran mitjançant tècniques convencionals i no-convencionals, emprant microones mono-modo i multi-mode. S'estudiaran diferents temperatures, i temps de manteniment. Com l'objectiu és veure l'efecte de cada paràmetre en la qualitat de les mostres finals obtingudes, es caracteritzaran els materials mitjançant microscòpia electrònica i assajos mecànics.

Paraules clau: Regolito llunar, regolito marcià, sinterització, microones, propietats estructurals.

Index

List of Figures

List of Tables

List of Equations

1. Introduction
1.1. Objectives of the project

The implementation of a permanent base on the Moon, and to a further extent on Mars appears as the logical next step of space exploration. In that purpose, space agencies foresee a human presence on the Moon within 20 years (Farries et al., 2021), and regolith is studied as raw material to build facilities. Different techniques are considered to shape this material, like additive manufacturing or sintering.

In this project, the sinterability of three regolith simulants is studied: the Lunar Highland Simulant LHS-1, the Lunar Mare Simulant LMS-1, and the Mars Global Simulant MGS-1. For that, conventional sintering, monomodal microwave and multimodal microwave sintering are used, with varying parameters such as sintering temperature and sintering time. Parameters affecting the green body are also tested, like compression force and granulometry.

Sintering is a process presenting many advantages. As melting is not reach, it necessitates lower energy and time, and it allows to keep the structure of the green body in case of specific shaping. The aim is therefore to find the optimal parameters to obtain good material properties.

1.2. Workplan

This project is divided in three main parts: green body creation, sintering and characterization of the sintered samples. The precise steps are:

First part:
- Milling of the simulants and measurement of their particle size distribution.
- Compacting of the powders with different parameters on a uniaxial press, to create green bodies.

Second part:
- Sintering in conventional oven with different sintering temperatures and times.
- Sintering in microwave oven with different potentials.

Third part:
- Hardness measurement to compare mechanical properties.
- Density measurement to verify sintering quality.
- Field Emission Scanning Electron Microscopy (FESEM) to observe the fracture section and the sintering stage of each sample thanks to porosity and grain size.

2. State of the art
2.1. Space

Extended research is realized to solve major problems coming with implanting human on others planet. For example, bringing raw material from Earth to another planet costs significantly, as one kilogram brought from Earth to the Moon costs 115k €. Consequently, using local resources, a concept known as In-Situ Resource Utilization (ISRU), is considered, and has become the spearhead of space manufacturing studies. Secondly, space environment imposes to protect astronauts and facilities from vacuum, radiations, extreme temperatures, dust, and meteoroids impacts. (Farries et al., 2021)

Concerning the Moon, multiple techniques, as additive manufacturing, sintering, or melting of regolith have been studied, and under different conditions like vacuum, air or hydrogen atmosphere (Farries et al., 2021; S. Taylor et al., 2018). Rovers to excavate and displace loose regolith like Cratos (Figure 1) are also developed. Besides, Moon regolith is planned to be used to produce oxygen. It was found that for the lowest yield, 415 kg of regolith can produce 1000 kg of oxygen (Caruso et al., 2008).

Figure 1: Cratos rover developped at NASA Glenn Research Center (Caruso et al., 2008).

Concerning Mars, a lot of manufacturing techniques, being sintering, melting, pressing, powder agglomeration, aggregate bonding and chemical fusion have been studied. Furthermore, the presence of clay resources on this planet is of particular interest for IRSU as it is a well-known material. The possibility to grow plants is also studied because required elements are present on Mars. Still, issues remain concerning the bioavailability and the quantity of these elements, as well as a possible toxicity. (Karl et al., 2022; Karl et al., 2020)

2.2. Materials
2.2.1. Lunar regolith

Lunar regolith is mainly composed of minerals, rocks, and glassy aggregates called agglutinates, which can contain iron nanophases. It was created by the impact of meteoroids and particles on the moon bedrock, provoking different mechanisms illustrated in Figure 2. A first one is that the impact led to the fragmentation of rocks and minerals. A second one is that the impact energy provoked instant melting of elements, Silicate for example. The melt generally quenched afterward, leading to glass

formation, but if the melt caught solid particles before quenching, it led to the formation of agglutinates visible in Figure 3. Agglutinates proportion in the lunar soil is significant, as it represents an average of 25-30 % (McKay et al. 1991).
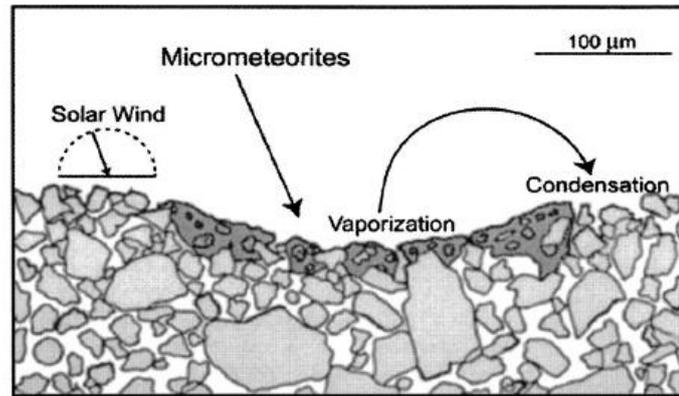
Figure 2: Schematic of the mechanisms occurring with the impact of a micrometeorite (L. Taylor et al., 2005).
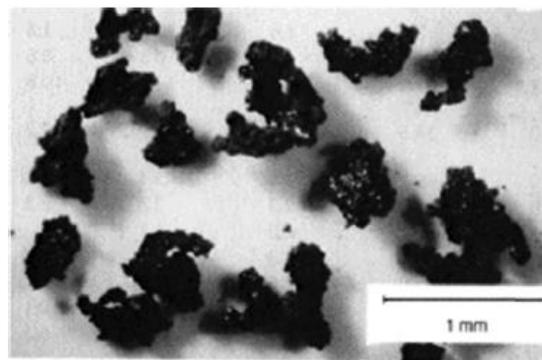
Figure 3: Agglutinates from Moon regolith (McKay et al. 1991).

Another mechanism is the reduction of FeO into native iron Fe^0 present in the agglutinates. When melting occurred, protons that had been implanted on particles surface by solar wind were liberated. These protons were then responsible of the reduction of FeO into Fe^0, which nucleated to form iron nanophase. The presence of native iron in regolith implies a strong magnetic susceptibility of the material (McKay et al. 1991; L. Taylor et al., 2005).

These mechanisms are responsible of a significant irregularity in particles shape, leading to specific area of 0.5 m²/g, synonym of a bad packing. Concerning the granulometry, grains with a diameter of less than 1 mm represent 95 wt%, 50 wt% for a diameter below 50 µm, and 15 wt% for grains below 20 µm (L. Taylor et al., 2005).

Besides, regolith composition of the Moon is not uniform and varies according to its origin. Two main regions, corresponding to two different origins, are defined (Figure 4):

- The highland region, which regolith was formed from an anorthositic curst rich in plagioclase feldspar ($CaAl_2Si_2O_8$). It is visible on the Moon as the light-coloured part, and its thickness has an average of 10-15m.

- The mare region, which regolith has a bigger quantity of pyroxene (($Ca,Mg,Fe)_2Si_2O_6$), olivine (($Mg,Fe)_2[SiO_4]$) and ilmenite ($FeTiO_3$) because it was formed from lava. It corresponds to the darkest part visible on the Moon, and its thickness is around 4-5 m (Farries et al., 2021; McKay et al. 1991).

Mare regolith also shows significant differences in Ilmenite (Titanium) content, and so high-Ti and low-Ti mare regions are distinguished (Farries et al., 2021).
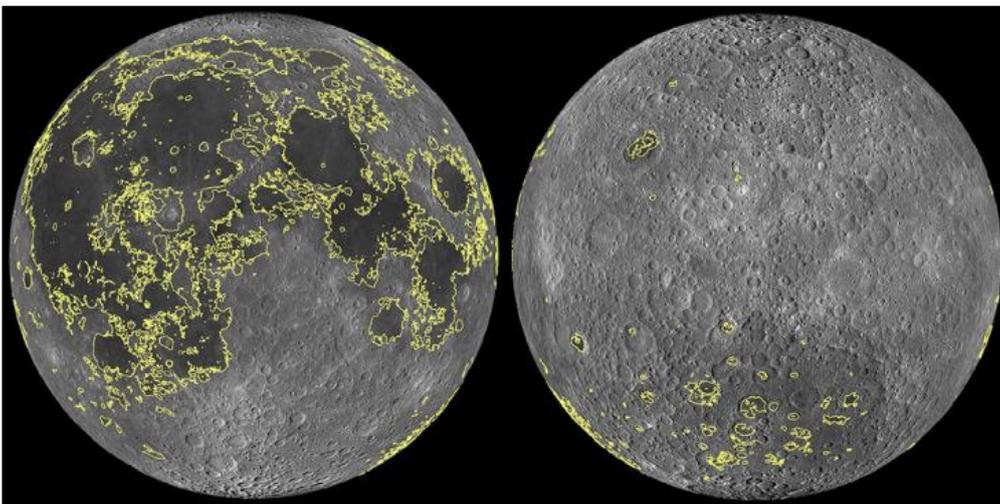
Figure 4: Images of each side of the Moon with marias circled in yellow (Farries et al., 2021).

2.2.2. Martian regolith

Mars has a long geological history, divided in four periods: Pre-Noachian, Noachian, Hesperian and Amazonian. This history resulted in the formation of different minerals and rocks, that are recorded in Mars soil. Thus, some regions of the surface can correspond to different periods and so, they show different compositions. For example, the northern hemisphere is mainly made of felsic rocks, containing silicium, oxygen or aluminium, while the southern hemisphere is manly composed of mafic rocks, which contains olivine or pyroxene. Still, the soil has an overall basaltic composition (Slyuta, 2014). Also, the interaction with water led to the formation of multiple clay resources, which appear to be interesting for ISRU (Karl et al., 2020).

Then, physical and chemical weathering, oxidation and interaction with liquid water led to the formation of regolith and dust that partly covers the surface. Figure 5 illustrates the abundance of dust on Mars, where the solid white line circles regions with abundant dust, and the dashed white line circles regions impoverished in dust. This regolith is consequently a mix of eroded and oxidized primary rocks (Slyuta, 2014). Even if it globally has a basaltic composition, some minerals content varies depending on the composition of the underlying bedrock (Cannon et al., 2019). For example, chemical

weathering made regolith poorer in olivine. Still, dunes were found with a bigger content of olivine, probably due to the local bedrock enriched in olivine. Besides, ferric oxydes and oxyhydroxides contained in the dust are responsible of the reddish colour of Mars (Slyuta, 2014). A picture taken by Curiosity on Mars is visible on Figure 6, showing regolith and rocky emergence.

Nevertheless, the knowledge of mineralogy relies on Mars rovers data and analysis, and is therefore limited by the characterisation techniques they contain (Slyuta, 2014). Consequently, it is to be enriched in the future.
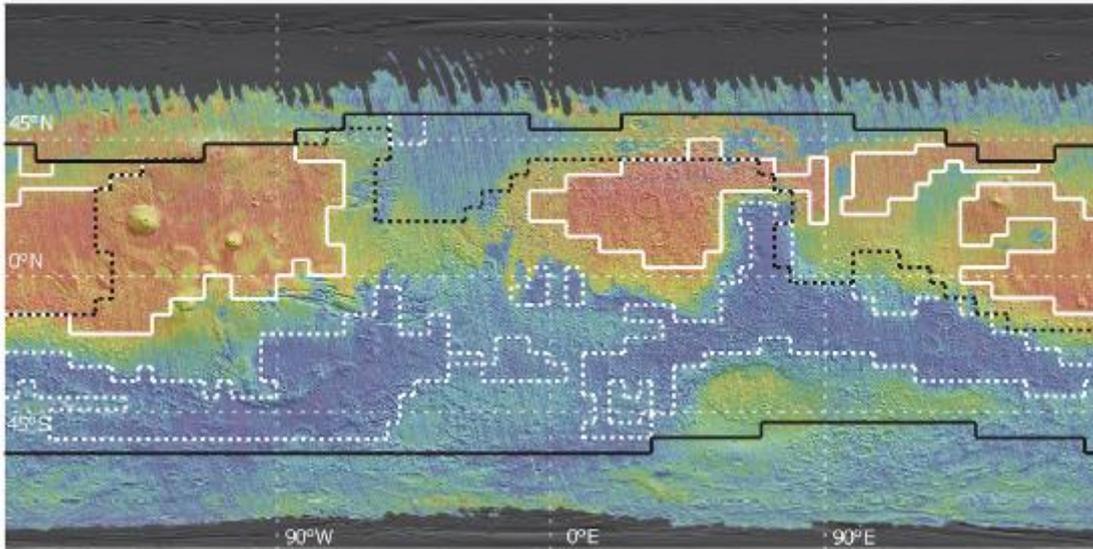
Figure 5: Map of Mars. Regions surrounded bysolid white boundaries are aboundant in dust, and regions surrounded by dashed white boundary are regions poor in dust (Certini et al., 2020).
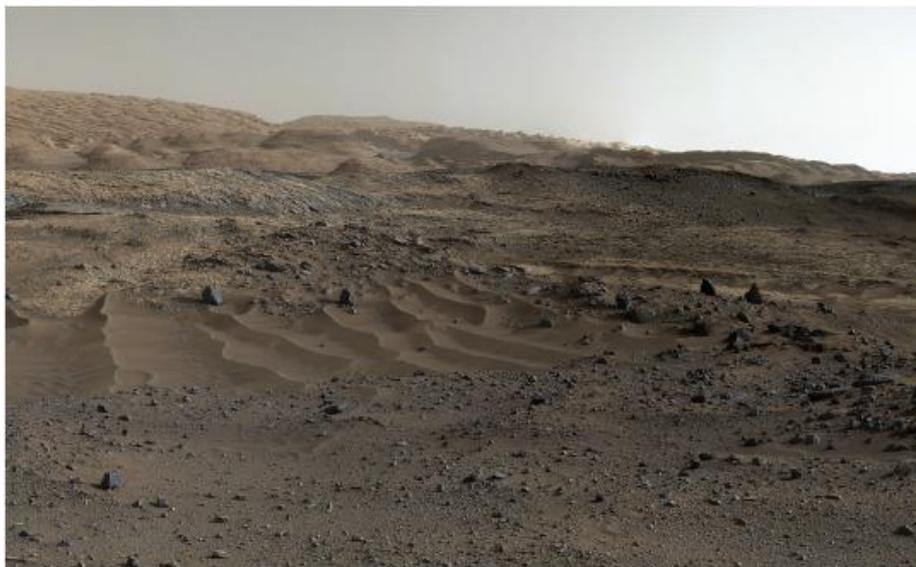
Figure 6: Picture of mars soil taken by Curiosity (Certini et al., 2020).

2.3.Sintering

Sintering is a method of forming materials. It consists of heating compacted powder, without reaching the material melting point. The driving force of any sintering mechanism is the reduction of the total energy of the system. But depending on the composition of the material, different mechanisms can occur.

2.3.1. Generalities
2.3.1.1. Solid-state sintering

In solid-state sintering, diffusion is the main mechanism leading to the cohesion of the green body. Three main steps characterized solid-state sintering.
The first one is the apparition and growth of bridges between grains, which can be caused by electrostatic forces or chemical bonds between superficial species. The contact between two grains can be represented as a torus with two curvature radiuses (a and b on Figure 7). The difference between them is responsible of a gradient of pressure in the surrounding gas, the lowest value being at the surface of the bond, as well as a stress gradient in the solid. These gradients will then lead to mass diffusion toward the bond surface (Bernache-Assolant & Bonnet, 2005a).

Depending on the matter source, the effect on the material structure will change. For example, matter diffusing from grain surface by gas transport, superficial diffusion or volume diffusion will lead to grain growth instead of densification because grains centers don't get closer. On the other hand, matter coming from grain boundary by volume or grain boundary diffusion will lead to densification (Borrell, Salvador, 2018). All mechanisms and their effect are summed up in Table 1 and illustrated in Figure 8.
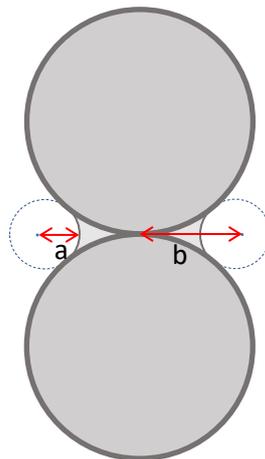
Figure 7: Schematic of two grains beginning to coalesce. The torus is characterized by radius a and b.
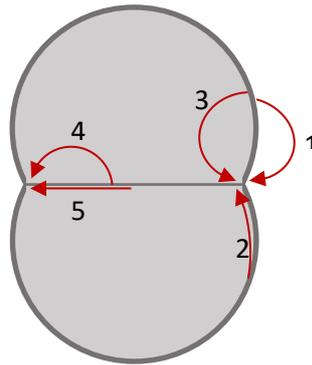
Figure 8: Schematic of transport mechanisms between two grains during sintering.

Table 1: Mechanisms of matter transport and their effect on the system (Borrell, Salvador, 2018).

Mechanism	Displacement nature	Source	Effect
1	Gaz transport	Grains surface	Grain growth/ consolidation
2	Superficial diffusion	Grains surface	Grain growth/ consolidation
3	Volume diffusion	Grains surface	Grain growth/ consolidation
4	Volume diffusion	Grain boundary	Densification
5	Grain boundary diffusion	Grain boundary	Densification
6	Plastic deformation	Volume	

Once bridges are formed, the structure is composed of linked grains that can be represented as cuboctahedrons bonded at the faces, and open pores located at their edges, as illustrated by Figure 9. The second step consists then of the elimination of these pores by volume or grain diffusion of matter, from face center to edges. This mechanism also leads to the densification of the material, as shown by the evolution of relative density with sintering time curve in Figure 10. At the end of this step only remains closed porosity at the grain corners (Bernache-Assolant & Bonnet, 2005a).

Open porosity
Closed porosity
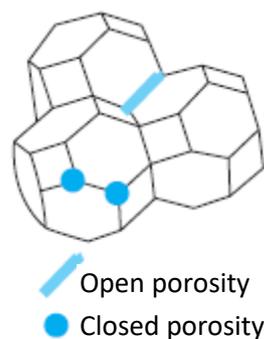
Figure 9: Schematic of open and closed porosity in the material (Bernache-Assolant & Bonnet, 2005a).
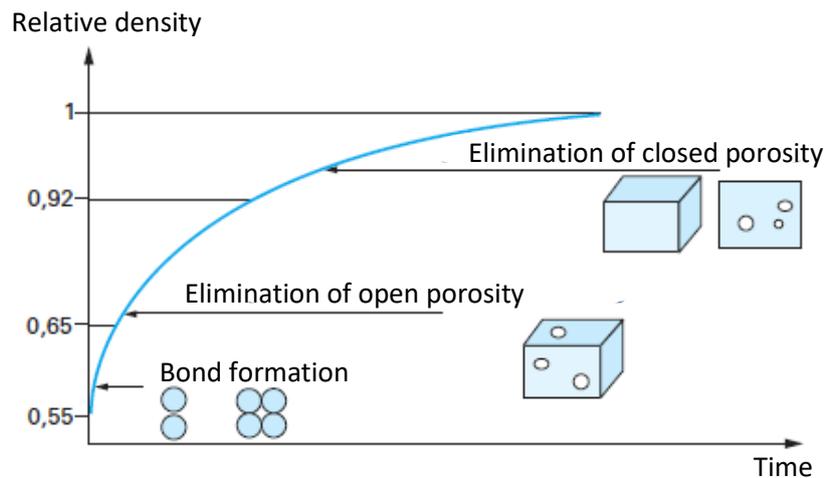
Figure 10: Evolution of relative density with the during sintering and the mechanism associated (Bernache-Assolant & Bonnet, 2005a).

Besides, microstructure modification is partly controlled by Laplace relation (Equation 1). It gives the pression in a grain P_i depending on its radius r and the solid/gas interface γ_{sg}. P_∞ is the saturation vapor pressure (Bernache-Assolant & Bonnet, 2005a).

$$P_i = P_\infty + \frac{2\gamma_{sg}}{r}$$

Equation 1: Laplace relation.

Laplace relation shows that a big grain will tend to reach P_∞, while small grains will be subjected to compressive stress. In the case of voids, r becomes negative, and so a small pore will be subjected to higher tensile stress. Consequently, small grain will tend to disappear for the benefit of bigger grains, as for voids (Bernache-Assolant & Bonnet, 2005a).

2.3.1.2. Liquid-state sintering

Liquid-state sintering is characterized by the formation of a liquid phase during sintering, and generally occurs when the green body is composed of different materials with different melting points. Heating provokes the melting of several elements, forming a liquid phase which quantity is generally below 5 %vol, but can reach 20 %vol (Borrell, Salvador, 2018). From that, three steps can be defined.

First, the liquid redistribution in the green body helps the rearrangement of solid particles. Indeed, it acts as a lubricant which allows the particles to slide on one another, leading to a reduction of the internal stress and of the solid/gas interfaces.

Second, the dissolution-precipitation mechanism occurs, driving the densification of the material. As for solid-state sintering, the curvature of the meniscus formed by the liquid phase between two grains creates a pressure gradient. The dissolution-precipitation mechanism will tend to reduce the curvature of the solid/liquid interface, causing densification of the material.

The final step is the elimination of voids coming with grain coalescence, due to the dissolution of small grains and their precipitation on bigger grains (Bernache-Assolant & Bonnet, 2005).
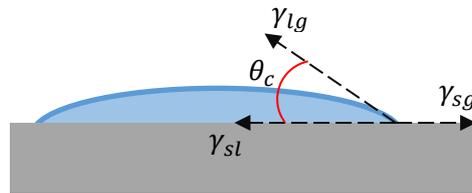
Figure 11: Schematic of the contact angle between the liquid and the solid.

The surface tension of the liquid phase is therefore a major factor in the sintering process. Indeed, a small contact angle (θ_c in Figure 11) between the solid and the liquid ensures a good wetting of the solid, and so a good repartition of the liquid in the green body (Borrell, Salvador, 2018).

However, the liquid phase causes the formation of an intergranular glassy phase, which therefore degrades the mechanical properties.

2.3.2. Non-conventional sintering: Microwave sintering

2.3.2.1. Matter/microwave interaction

Three main categories of material are defined considering their interaction with microwaves (Borrell, Salvador, 2018):

- Transparent materials in which the microwaves pass without energetic loss (Figure 12a). Alumina fiber is a transparent material for example.
- Absorbent materials which absorb waves energy, depending on the loss factor value (Figure 12b). For example, Silicium Carbide.
- Opaque materials on which the waves are reflected (Figure 12c), this is the case of metals.
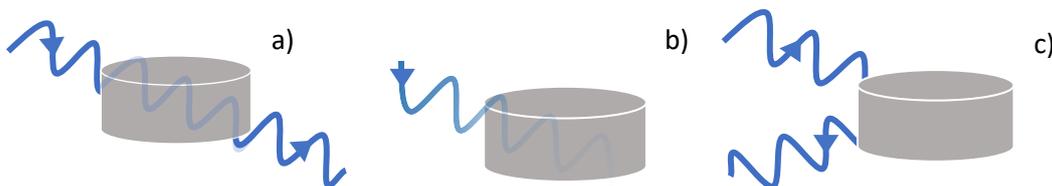
Figure 12: Schematics of matter/wave interaction of a) transparent materials, b) absorbent materials, c) opaque materials.

In the case of absorbent materials, the interaction between a material and a microwave can be expressed with too values. First, the absorbed power P, defined in Equation 2, corresponds to the amount of energy absorbed by the material. In this expression, f is the radiation frequency, E is the electric field intensity, ε_0 the vacuum permittivity and ε' the dielectric constant of the material (Borrell, Salvador, 2018).

$$P = \sigma|E|^2 = 2\pi f \varepsilon_0 \varepsilon' \tan\delta \ |E|^2$$
Equation 2: Power absorbed by the material.

$$\tan\delta = \frac{\varepsilon''}{\varepsilon'}$$
Equation 3: Loss tangent.

Equation 3 is the loss tangent, in which the loss factor ε'' measures the ability of a material to transfer electromagnetic energy into heat. The dielectric constant ε' corresponds to the ability of a material to polarize. Those two values depend on temperature and wave frequency (Borrell, Salvador, 2018).

Second, the depth of microwave penetration D, corresponds to the depth at which the power is reduced by half in the material, and is expressed in Equation 4.

$$D = \frac{2\pi_0}{8.686 \ \pi \tan\delta \left(\frac{\varepsilon'}{\varepsilon_0}\right)^{1/2}} = \frac{C}{2\pi f \sqrt{2\varepsilon'}\left(\sqrt{1 + tan^2\delta - 1}\right)^{1/2}}$$
Equation 4: Penetration depth of microwave in a material.

Equation 4 shows that high frequency and high dielectric properties lead to a smaller value of D, and so superficial heating. Consequently, to favor a homogeneous penetration of waves in the material, lower frequencies and lower dielectric properties are preferred (Borrell, Salvador, 2018).

2.3.2.2. Heating mechanisms

Different mechanisms lead to heating at macroscale, being bipolar rotation, resistive heating, electromagnetic heating, and dielectric heating (Borrell, Salvador, 2018).

- Bipolar rotation occurs in polar molecules like water. Under the oscillating magnetic field, charges start to rotate and create molecular friction leading to heat.

- Electromagnetic heating occurs in material with high magnetic susceptibility. As for bipolar molecules, the oscillating waves provoke a rotation of the magnetic poles, and heat.

- Resistive heating occurs in conductive materials with high electric resistivity, in which electrons or ions have enough liberty to move and generate current leading to heat.

- Finally dielectric heating is a mix of bipolar rotation and resistive heating.

In the case of a mix of materials with different dielectric properties, the heating behavior is difficult to predict, and the general heating method should be adapted. Thus, three main heating methods exists. First, when the material interacts well with the radiation, direct coupling provokes volumetric heating. In that case, a temperature gradient appears from the center to the surface of the material, in contact with the cooler atmosphere, as illustrated by Figure 13a**.**

In the case of a material with poor dielectric properties at low temperature, susceptors with good dielectric properties like Silicium Carbide can be used to create hybrid heating. At low temperature, it will absorb a major part of the microwave and transmit heat to the green body by infrared. At higher temperatures, when the dielectric properties of the green body are better, it will couple with the microwaves and heat by direct heating. As shown in Figure 13b hybrid heating presents the most homogenous heating as the chore and the surface are both heated.

Finally, if the green body has poor dielectric properties at high temperature too, susceptors will absorb a major part of the microwaves and transmit heat to the green body during all the process. This indirect heating leads to a temperature gradient from the surface to the chore of the sample (Figure 13c) (Borrell, Salvador, 2018).
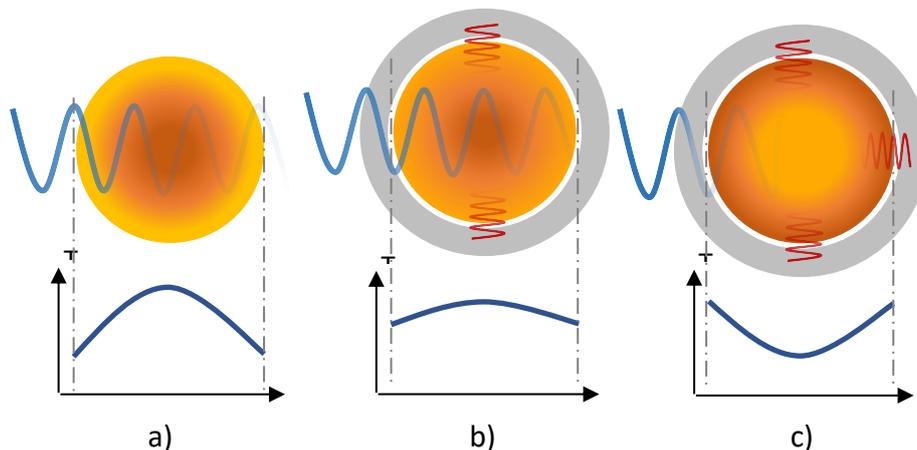
Figure 13: Schematic and temperature profile in the material during a) direct heating, b) hybrid heating, and c) indirect heating.

2.3.2.3. General description of the microwave oven

Three main parts compose a single mode microwave oven. The microwave source, the resonant cavity in which the sample is placed, and in between the transmission line guiding the wave. The microwave source is a magnetron, which transforms electric energy into high frequency electromagnetic energy. The frequency generally used is 2.45 GHz. Regarding the resonant cavity, in single mode its size should be of the order of the wavelength, and its length can be tuned. Then, other features complete the oven (Borrell, Salvador, 2018):

- The circulator, which role is to redirect waves reflected by the sample to the water circuit. By absorbing it, the water protects the microwave source.
- The reflectometer measures the potential of the reflected energy. This allows to reach a true value of the absorb potential.

- The iris is used to couple the microwave potential into the cavity.
- The pyrometer, which is not part of the oven but is added, is used to measure the temperature of the sample during the process.

All the elements of the oven are illustrated in Figure 14.
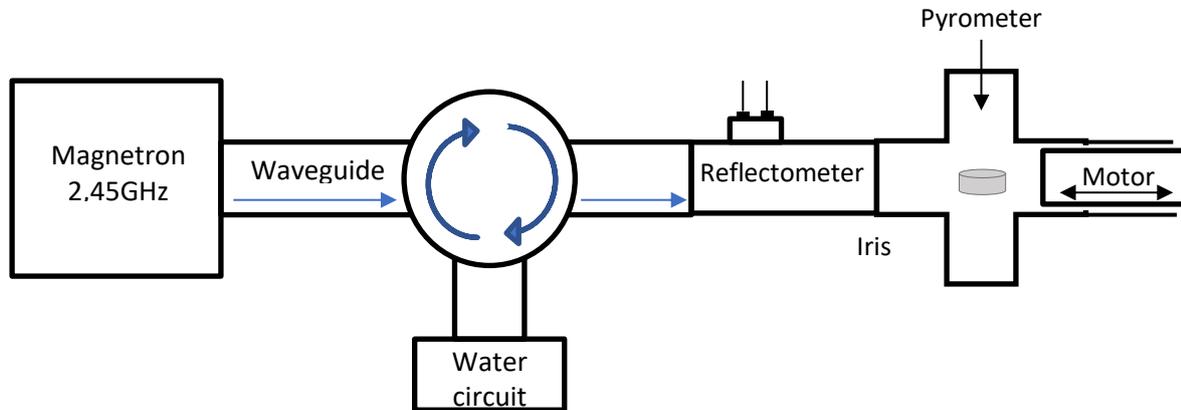
Figure 14: Schematic of a monomodal microwave oven.

3. Equipment techniques and method
3.1. Green body preparation
3.1.1. Milling

The simulants were ground with the planetary ball mill Fritsch Pulverisette to study the impact of grain size distribution. In the grinding bowls (Figure 15, left) were placed 4 g of powder, 40 g of Alumina balls (5mm diameter), and 33 g of isopropanol to avoid the formation of agglomerates. The corresponding balls/powder ratio is 10:1, and the isopropanol mass represents 75 % of the total mass of balls and powder. Two settings were used, a first one at 800 rpm for two hours with reversal, and a second one at 400 rpm for one hour with reversal. The parameters are detailed in Table 2. After milling, the powders were dried in an oven and sieved in a 63 µm mesh (Figure 15, right).

Try	Rotation per minutes (rpm)	Timer (min)	Pause (min)	Cycles	Revers
1	800	30	10	2	On
2	400	30	10	1	On

Table 2: Milling parameters.

Figure 15: Image of the grinding bowls after milling on the left and sieving of the powder on the right.

3.1.2. Compaction

Green bodies were realized with milled and raw powders, because compacting helps the sintering process. For that, powder was placed in a cylindrical mold before being pressed in a uniaxial press shown in Figure 16. The samples were subjected to 2.5 t or 5 t for two minutes, and then demolded. At the end, green bodies of 12 mm diameter and between 50 and 100 mm height were obtained.

Figure 16: Image of the uniaxial press on the left, and of the demoulding press on the right.

3.2. Sintering techniques
3.2.1. Conventional sintering

Conventional sintering was realized with Carbolyte Gero high temperature laboratory furnace (Figure 17). All green bodies were sintered in air and with a heating rate of 10 °C/min. First, sintering temperature of 700 °C, 900 °C, 1000 °C and 1100 °C were used with the three raw simulants, as well as 1200°C for LHS simulant, and the sintering time was set at one hour. Considering the results obtained, sintering temperatures of 1000°C and 1100°C were chosen for milled simulants, during one or two hours. This decision will be explained in the results and discussion (Chapter 4.2.1). Each time, a

Sinterability study of lunar and Martian regolith simulants by conventional and non-conventional methods.

Process Temperature Control Ring was used to control the temperature reached in the oven. Table 3 gathers all parameters applied on each powder.

Figure 17: Carbolite Gero high temperature furnace used for conventional sintering.

Table 3: Sintering parameter combinations applied in conventional sintering.

Material	Milling (rpm/h)	Compression (t)	Sintering method (in air)	Sintering (T°)	Sintering time (h)
LHS	---	2.5	CS	700	1
	---	2.5	CS	900	1
	---	2.5	CS	1000	1
	---	2.5	CS	1100	1
	---	2.5	CS	1200	1
	400	5	CS	1000	1
	400	2.5	CS	1000	1
	400	2.5	CS	1100	1
	400	2.5	CS	1100	2
LMS	---	2.5	CS	700	1
	---	2.5	CS	900	1
	---	2.5	CS	1000	1
	---	2.5	CS	1100	1
	400	5	CS	1000	1
	400	2.5	CS	1000	1
	400	2.5	CS	1100	1
	400	2.5	CS	1100	2
MGS	---	2.5	CS	700	1
	---	2.5	CS	900	1
	---	2.5	CS	1000	1
	---	2.5	CS	1100	1
	400	5	CS	1000	1

	400	2.5	CS	1000	1
	400	2.5	CS	1100	1
	400	2.5	CS	1100	2

3.2.2. Microwave sintering
3.2.2.1. Monomodal microwave

Microwave sintering was realized with a monomodal microwave device designed by ITACA-UPV (Instituto de Aplicaciones de las Tecnologías de la Información y de las Comunicaciones Avanzadas) and ITM-UPV (Instituto de Tecnología de Materiales) that can be seen in Figure 18. The sample was placed in a quartz tube and surrounded by Alumina fibre. When a susceptor was needed, Silicium Carbide was placed below the sample and separated from it with a disc of Alumina fibres as illustrated by Figure 19. The tube was then placed in the resonant cavity.

Figure 18: Microwave oven designed at ITACA-UPV.
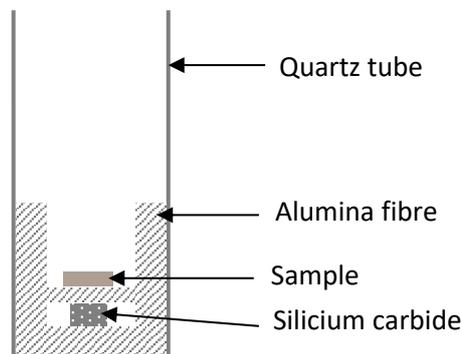
Figure 19: Schematic of the elements placed in the resonant cavity of the microwave oven.

At the beginning of the process, the material emissivity and transmissivity are put in the software. The tuning position, which is the motor position, is set at its minimum, and the generator is turned on. Then, the tuning position is gradually adapted to optimize the sample/microwave interaction. The

dependence of the temperature on the tuning position can be represented as a gaussian curve. The aim is consequently to know the first half of the curve and so the maximum temperature that can be reached (equivalent to the absorbed power) by adapting the tuning position. Once it is reached, the tuning position still has to be adapted to keep the maximum temperature during the sintering time. The power was set between 300 W and 500 W.

3.2.2.2. Multimodal microwave

Sintering in multimodal microwave was also attempted. For that, a domestic microwave Sharp YC-MG81E-S was used (Figure 20), which maximum potential is 900 W. The sample was placed on Alumina fibres in the centre of the oven, and potentials between 270 W and 900 W were used, during 3 to 20 minutes.

Figure 20: Outside and inside of the multimodal microwave oven.

3.3. Sample preparation

Once the sintered samples obtained, they had to be cut, fixed in resin and polished to be able to analyze them.

3.3.1. Cutting and coating

Cutting was realized to subsequently analyze the chore of the sample with hardness and FESEM and to have a plane surface. A REMET manual cutting saw from Someco equipped with a diamond disk 0.4 mm thick was used (Figure 21). After that the pieces were fixed in thermoplastic resin.

Figure 21: Circular cutting machine.

3.3.2. Polishing

The samples, previously fixed in thermoplastic acrylic, were all polished with the same procedure, which are summed up in Table 4. This allows to reduce the surface rugosity prior to Vickers hardness.

Table 4: Polishing steps.

Grains (µm)	Time (min)	Lubricant	RPM	Force (N)
75	5	Water	100	10
40	1	Water	100	10
20	1	Water	100	10
10	1	Water	100	10
6	10	Diamond suspension 6 µm	150	20
3	8	Diamond suspension 3 µm	150	20
1	8	Diamond suspension 1 µm	150	20

3.4. Powder characterization
3.4.1. Emissivity

Emissivity depending on temperature is necessary to perform monomodal microwave sintering, and therefore had to be measured for the three simulants. For that, a green body of each powder was made to be placed in the oven afterwards. Once the sample placed in the oven, emissivity at 600 °C, 700 °C, 800 °C, 900 °C and 1000 °C were measured with the pyrometer LT-CF3-CB3, using the setting

illustrated in Figure 22. The heating rate was 10 °C/min with a 5 min dwell for each emissivity measure, and the transmittivity was set at 1.1.
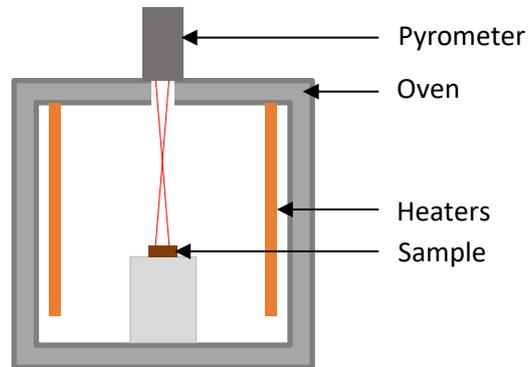
Figure 22: Schematic of the display used to measure emissivity.

3.4.2. Particle size distribution

Particle size distribution of raw simulants and milled simulants was measured with the Malvern Panalytical Mastersizer 2000 by laser diffraction (Figure 23). A small quantity of powder was poured in the dispersion unit with distilled water, and then joined the distilled water circuit. Once dispersed, grain particles pass through a focused laser beam, which is therefore diffracted. Detectors capture the diffracted light and from the angle and the intensity the particle size can be determined. Three measures are realized for each powder. Still, particle agglomerates poured in the circuit may not disintegrate and so leading to an overestimation of particle sizes.

Figure 23 : Malvern Panalytical Mastersizer 2000, with the dispersal unit in the centre.

3.5. Samples characterization
3.5.1. Density

Density of the powders had been previously measured with a He pycnometer. Therefore, measuring the true density of each material would allow to calculate relative density as well as porosity of the material, giving an indicator of the sintering quality. For that, Archimedes' method was used.

The samples were put in distilled water and heat up for at least three hours before being left in water for a night. Mass of the wet samples was then measured, given $W(fl)$. Next, the samples were dried in an oven for a day and the mass of dry samples was measured, giving $W(a)$. From that, density was calculated with Equation 5, where $\rho(fl)$ is the density of water at room temperature.

$$\rho = \frac{W(a).\rho(fl)}{W(a) - W(fl)}$$

Equation 5: Archimedes' density formula.

3.5.2. Microhardness

Microhardness was measured with the Vickers hardness test on a portative durometer (Figure 24). In Vickers test the penetrator is a diamond in the form of a square-based pyramid. Hardness is calculated with the dimensions of the mark left by the indent on the material. At least five measures were realized and aberrant values were suppressed to obtain a reliable average value.

Figure 24: Portative durometer

3.5.3. Field Emission Scanning Electron Microscopy (FESEM)

Electronic microscopy takes advantage of the electron/matter interaction to obtain a topography of the analyzed surface. Indeed, a surface subjected to an electron beam produces secondary electrons, backscattered electrons and specific X-rays, which signals will change accordingly to the phases or the topography on which the electron beam is focused (Mutalib et al., 2017). In this project, FESEM (Figure 25) was specifically used for its high spatial resolution. The samples were fractured before being observed. The aim was to measure grain size and fracture type afterward.

Figure 25: Field Emission Scanning Electron Microscope

4. Characterization and results
4.1.Raw materials

The quantity of regolith brought back on Earth from the moon is limited, and none has been brought back from Mars. For these reasons, simulants had to be created to allow further investigations. Simulants are designed to reproduce the composition (chemistry and mineral) and granulometry as well as possible. Still, as they are made with Earth resources and elements, they can present differences with the true composition that must be considered. In this project, simulants from Exolith Lab were used. Specifically:
- Lunar highland simulant LHS-1
- Lunar mare simulant LMS-1 were used for Moon regolith
- Mars global simulant MGS-1 was used.

4.1.1. Lunar regolith simulants

Compositions of LHS and LMS are summed up in Table 5 and 6. They are similar at first sight, and both have a significant amount of glass rich basalt. LMS is richer in Pyroxene, Olivine and Ilmenite, giving its darker colour, while LHS is richer in Anorthosite, giving its lighter colour.

Then, Exolith Lab gives major differences between simulants and true regolith. In terms of shape, simulants particles may not be as smooth as eroded regolith particles, as well as not angular enough compared to agglutinates for example. In terms of composition, simulants have more ferric iron and do not have iron nanophase. Furthermore, they may have excesses in magnesium, sodium and potassium, and deficiencies in iron and calcium due to terrestrial material specificities. Finally, simulants are not subjected to lunar weathering, and are stabilize with terrestrial atmosphere which has more oxygen and humidity than the Moon. This means that simulants are less reactive to these two elements compared to space material (Exolith Lab, n.d.).

Table 5: LHS and LMS components.

Component	LMS (wt.%)	LHS (wt.%)
Anorthosite	19.8	74.4
Pyroxene	32.8	0.2
Glass rich basalt	32	24.7
Olivine	11.1	0.3
Ilmenite	4.3	0.4

Table 6: LHS and LMS oxydes.

Oxyde	LMS (wt.%)	LHS (wt.%)
SiO_2	40.2	48.1
Al_2O_3	14	25.8
CaO	9.8	18.4
Fe_2O_3	13.9	3.7
K_2O	0.6	0.7
MgO	12	0.3
MnO	0.3	0.1
P_2O_5	1	1
TiO_2	7.3	1.1
Cl	0.4	0.4
SrO	0.1	0.1
Cr_2O_3	0.3	---
NiO	0.2	---
SO_3	---	0.3

4.1.2. Mars regolith simulants

Components and oxides composition of MGS are summed up in Table 7 and 8. This simulant was designed to reproduce the globally basaltic regolith (Exolith Lab, n.d.). As explained in a previous part, Mars geology is rich and has led to an inhomogeneous surface composition locally enriched in certain elements. Consequently, MGS does not represent local composition specificities, and results obtained with it correspond to an average behaviour that can varies with true Martian regolith, depending on its region.

Table 7: MGS components.

Component	MGS (wt.%)
Anorthosite	27.1
Pyroxene	20.3
Glass rich basalt	22.9
Olivine	13.7
Ilmenite	---
Mg sulfate	4
Ferrihydrite	3.5
Hydrated silica	3
Magnetite	1.9
Anhydrite	1.7
Fe-carbonate	1.4
Hematite	0.5

Table 8: MGS oxydes.

Oxyde	MGS (wt.%)
SiO_2	45.2
Al_2O_3	14.9
CaO	10
Fe_2O_3	18.7
K_2O	0.6
MgO	7.6
MnO	0.1
P_2O_5	0.9
TiO_2	0.4
Cl	0.4
SrO	0.1
Cr_2O_3	0.2
NiO	0.2
SO_3	0.9

4.2. Preparation
4.2.1. Milling

A first attempt was realised with LHS and LMS powders at 800 rpm for two hours (Table 2). After milling and drying for a night, a mass transfer of 10 g between the Alumina balls and the powders was noted. A second attempt was therefore realised at 400 rpm during 1 h and was conclusive. These second parameters were consequently kept for further milling.

Images of the powders before and after milling are visible in Figure 26 and Figure 27, respectively. Big darker grains in raw powders could be distinguished, some are visible in Figure 26b, and no agglomerates were formed. On the contrary, after milling no bigger grains were visible. The powders appeared very fine and agglomerates appeared, as visible on Figure 27.

a)   b)   c)
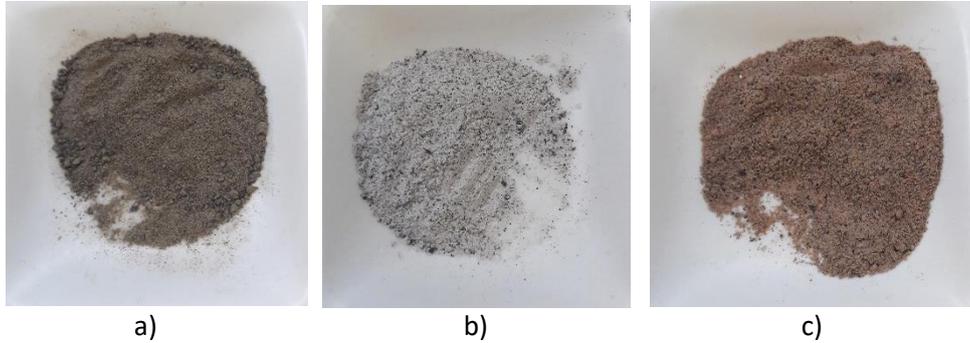
Figure 26: a) raw LMS, b) raw LHS, c) raw MGS.

a)   b)   c)
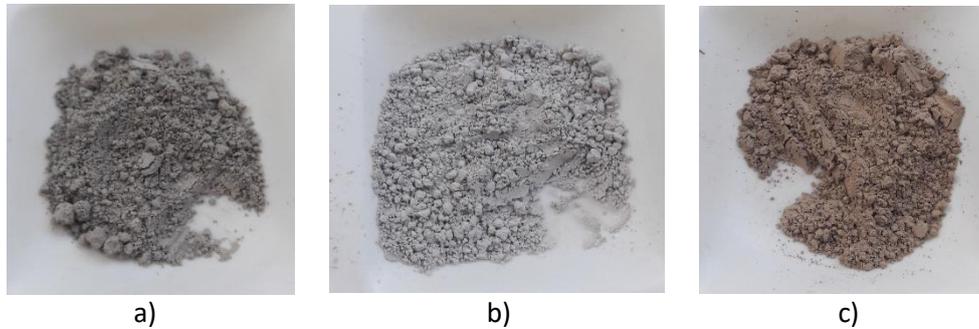
Figure 27: a) milled LMS, b) milled LHS, milled MGS.

4.2.2. Particle size distribution
4.2.2.1. Lunar simulants
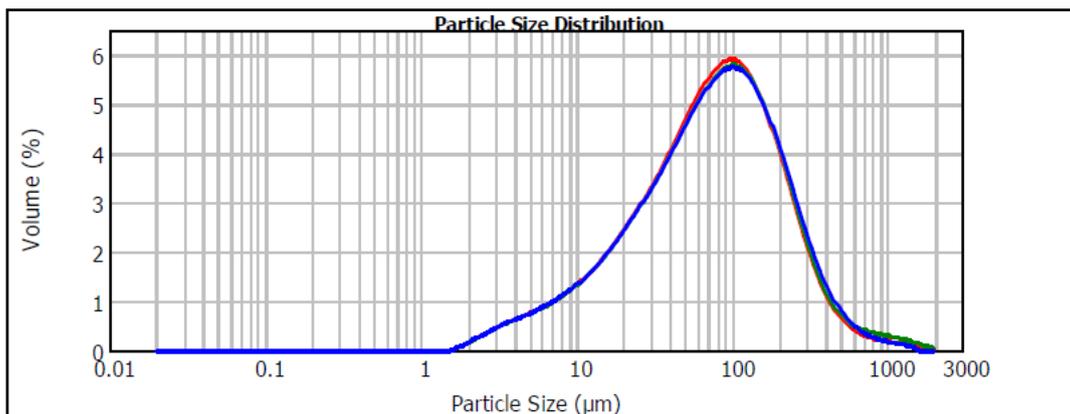
Figure 28: Particle size distribution of LHS simulant before milling.
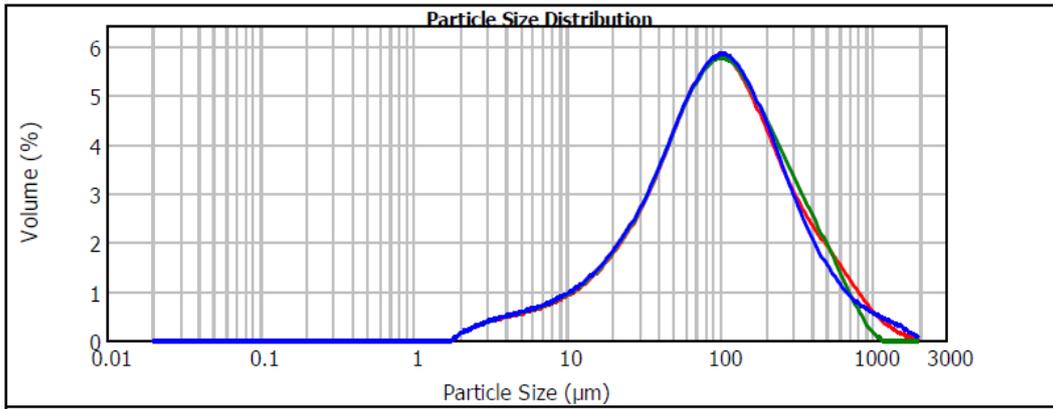
Figure 29: Particle size distribution of LMS simulant before milling.

Raw LMS and LHS (Figure 28 and 29) show similar grain size distribution, with a maximum diameter of about 1100 µm, a peak at 100 µm and a minimum between 1.5 and 2 µm. A ledge is visible between 3 and 10 µm, and is more pronounced for LMS-1. Another ledge is visible on LHS curve between 600 and 1050 µm.
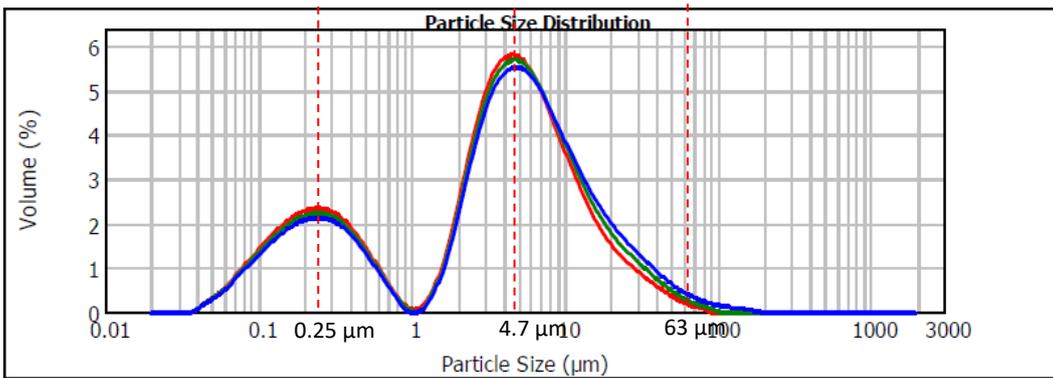
Figure 30: Particle size distribution of LHS simulant after milling.
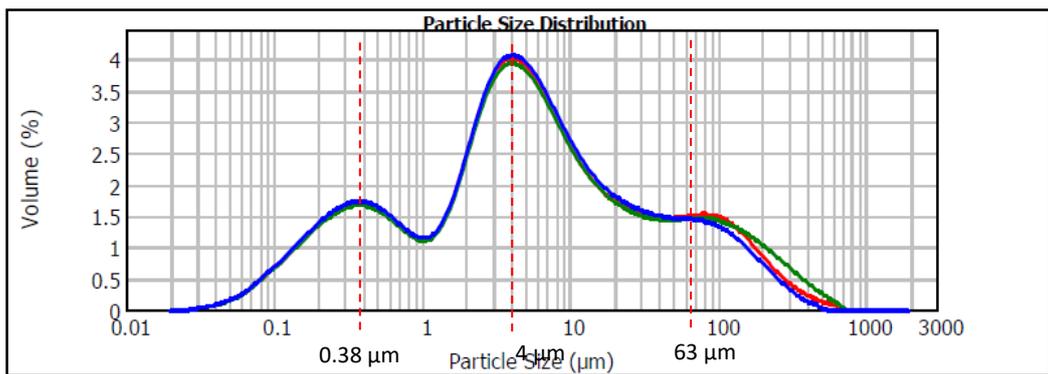
Figure 31: Particle size distribution of LMS simulant after milling.

After milling and sieving the powders, curves Figure 30 for LHS and 31 for LMS were obtained. The grain size range changed, being approximately [0.04;100] µm for LHS and [0.02;700] µm for LMS. A displacement of the maximum peak at 4.7 µm for LHS, and 4 µm for LMS occurred, while a secondary peak also appeared on both curves, at 0.25 µm for LHS, and at 0.38 µm for LMS. Milling consequently

led to the formation of grain of less than 1 μm diameter, and to a significant reduction of grains of more than 100 μm diameter.

Besides, after sieving in a 63 μm mesh few grains bigger than the mesh remain for LHS powder. However, on LMS curve a ledge is visible between 50 and 80 μm, and negligible volume can only be considered from 600 μm. The volume of grains bigger than 63 μm may be explained by an unvoluntary mix of raw powder with milled powder.

Between the two maximum peaks is a minimum at 1 μm, on LHS and LMS curves. This bimodal distribution can be due to the fracture of the bigger grains into small pieces, while small grains remained intact. However, it is important to consider that particles agglomerates might have remained in the water circuit and therefore their diameter had been measured instead of individual grain.

4.2.2.2. Mars simulant
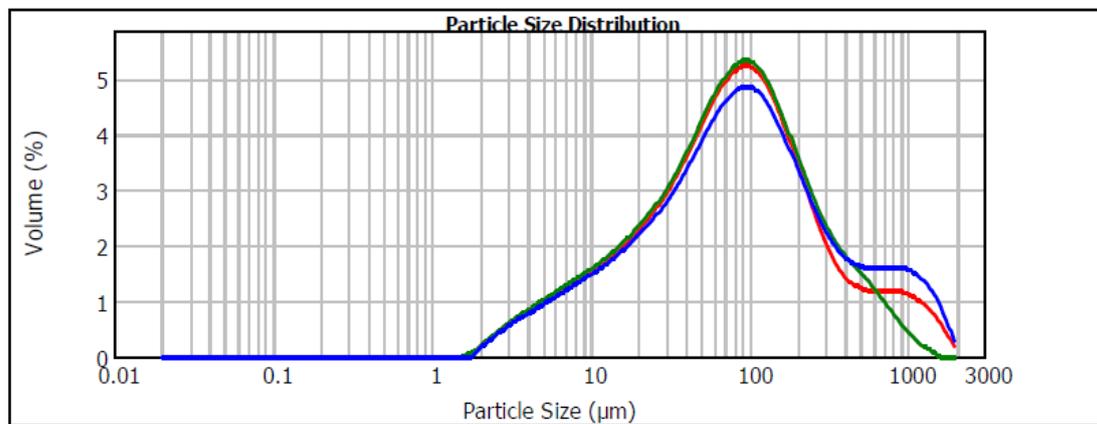
Figure 32: Particle size distribution of MGS simulant before milling.

For raw MGS (Figure 32), there is a peak at 100 μm, and the value range is between 1.7 and 1100 μm. A small ledge appears between 500 and 1000 μm.
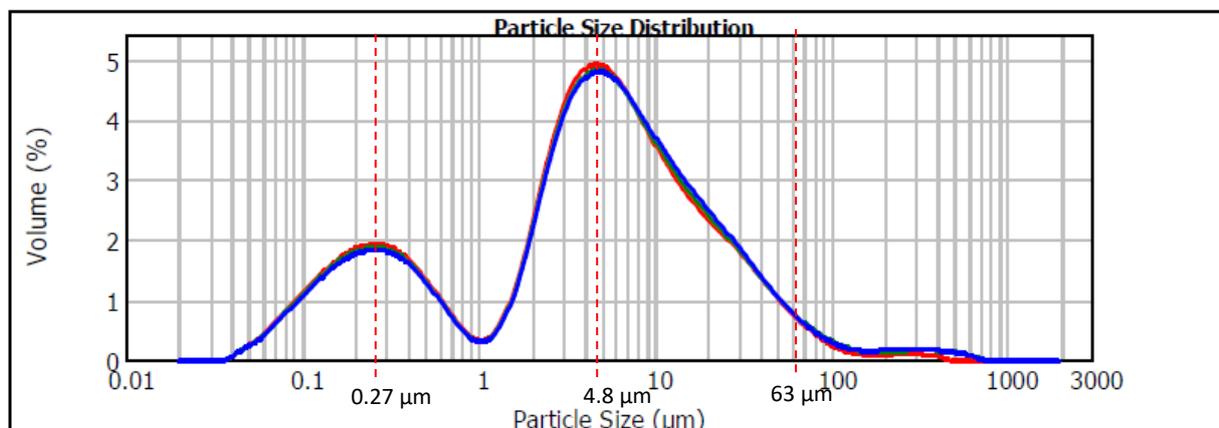
Figure 33: Particle size distribution of MGS simulant after milling.

After sieving a bimodal distribution appeared on Figure 33, with a first peak at 4.8 µm, and a second at 0.27 µm. A local minimum is also for 1 µm grain size. Thus, a clear reduction of grain sizes can be observed with a displacement of the maximum peak and the apparition of the secondary peak. However, a small proportion of grain between 100 µm and 700 µm remains after sieving.

4.2.3. Compression

Moulding and compressing of the powder gave cylindrical green body of 12 mm diameter and around 5 mm length. After demoulding, a metallic layer formed by the mould remained on the sample and had to be removed. Generally, the green bodies were fragile as they often break in two pieces during demoulding or polishing, regardless of the applied force. A layered structure was noticed. Figure 34 shows LMS and MGS samples that broke during demoulding. The metallic layer is visible on the edge of the two samples, and the layered structure can be perceived on the upper part of MGS sample. Figure 35 shows a sample of each milled simulant after removing the metallic layer. This did not occur when compressing unmilled powder, still the samples were more friable. Figure 36 shows samples made of raw simulant just after demoulding. No metallic layer is formed, but they are friable as illustrated by grains around the sample in Figure 36b.

Figure 34: Broken LMS (left) and MGS (right) green body made with milled simulants.

Figure 35: LHS (left), LMS (center), MGS (right) green body made with milled simulants.

Figure 36: LHS (left), LMS (center), and MGS (right) green body made with unmilled simulants.

4.3. Sintering process
4.3.1. Conventional sintering

4.3.1.1. Lunar simulants

First, raw LHS and LMS were sintered at 700, 900, 1000 and 1100 °C. Figure 37 shows LMS samples sintered at the four previous temperatures (from left to right) and heated in distilled water for three hours. The water corresponding to 700 °C sintering temperature resulted clouded, and a deposit is visible. As for 900 °C sample, a significant deposit is visible in the beaker. The same results were obtained with LHS samples. This mean that the samples subjected to 700 and 900 °C did not sinter, and it was decided that sintering temperatures of 1000 and 1100 °C would be applied to all following samples. Table 9 gathers all lunar samples sintered in conventional method that could be analysed, with their name.

Figure 37: Samples made of raw LMS and heated 3 hours in distilled water. They were sintered in conventional oven at (from left to right) 700, 900, 1000 and 1100 °C.

Table 9: All lunar sintered samples that could be analysed and their name.

Material	Milling (rpm/h)	Compression (t)	Sintering method (in air)	Sintering Temperature (°C)	Sintering time (h)	Name
LHS	X	2.5	CS	1000	1	LHS-2.5-CS1000/1
	X	2.5	CS	1100	1	LHS-2.5-CS1100/1
	X	2.5	CS	1200	1	LHS-2.5-CS1200/1
	400	5	CS	1000	1	LHSm-5-CS1000/1
	400	2.5	CS	1000	1	LHSm-2.5-CS1000/1
	400h	2.5	CS	1100	1	LHSm-2.5-CS1100/1
	400	2.5	CS	1100	2	LHSm-2.5-CS1100/2
LMS	X	2.5	CS	1000	1	LMS-2.5-CS1000/1
	X	2.5	CS	1100	1	LMS-2.5-CS1100/1
	400	5	CS	1000	1	LMSm-5-CS1000/1
	400	2.5	CS	1000	1	LMSm-2.5-CS1000/1
	400	2.5	CS	1100	1	LMSm-2.5-CS1100/1
	400	2.5	CS	1100	2	LMSm-2.5-CS1100/2

As can be seen on Table 10 and 11, which gathers images of sintered samples of LHS and LMS, samples turned red during sintering with a more pronounced colour for LMS samples. This can be due to the presence of iron oxide (Fe_2O_3) in both compositions, with a bigger proportion in LMS simulant. Furthermore, lighter phases are visible on sintered samples of milled LMS. As their colour is similar to LHS sintered sample, they can correspond to anorthosite minerals.

Table 10: Images of LHS samples after conventional sintering.

LHS	Unmilled powder	Milled powder
1000°C/1h		
1100°C/1h		

Table 11: Images of LMS samples after conventional sintering.

LMS	Unmilled powder	Milled powder
1000°C/1h		
1100°C/1h		

When sintering LHS at 1200 °C, LHS-2.5-CS1200/1 resulted in a dark sample with a glassy aspect (Figure 38, right). An overheating that led to a bigger quantity of liquid-phase, and a modification of the composition may have occurred. From that, the maximum sintering temperature for conventional sintering was set as 1100 °C.

Figure 38: LHS-2.5-CS1100/1 (left) and LHS-2.5-CS1100/1 (right).

Besides, sintered samples with unmilled powder were more friable compared to sintered samples with milled powder. This mean that for samples made of unmilled powder, the sintering time was not long enough to reach a sintered structure. It also led to a first hypothesis that a finer granulometry allows a better cohesion of the sample, and so possibly better sintering properties.

4.3.1.2. Mars simulant

Similarly to lunar simulants, samples made of raw MGS and subjected to 700 and 900 °C resulted friable and not sintered. Consequently, 1000 and 1100 °C sintering temperatures were also kept for all other samples. Table 12 gathers all names of MGS samples sintered in conventional method that could be analysed.

Table 12: Mars samples sintered in conventional way that could be analysed and their name.

Material	Milling (rpm/h)	Compression (t)	Sintering method (in air)	Sintering Temperature (°C)	Sintering time (h)	Name
MGS	X	2.5	CS	1000	1	MGS-2.5-CS1000/1
	X	2.5	CS	1100	1	MGS-2.5-CS1100/1
	400	5	CS	1000	1	MGSm-5-CS1000/1
	400	2.5	CS	1000	1	MGSm-2.5-CS1000/1
	400	2.5	CS	1100	1	MGSm-2.5-CS1100/1
	400	2.5	CS	1100	2	MGSm-2.5-CS1100/2

MGS samples also turned red with more intensity due to the presence of iron oxide, as visible in Table 13. Samples made of unmilled powder were also friable because the material was not sintered enough.

Table 13: Images of MGS samples after conventional sintering.

MGS	Unmilled powder	Milled powder
1000°C/1h		
1100°C/1h		

4.3.2. Microwave sintering
4.3.2.1. Monomodal microwave

Emissivity of the three simulants was first measured, and the values are summed up in Table 14. A first attempt was realised with a green body made of milled LMS, surrounded with alumina fibre, as illustrated by Figure 39.1. The temperature sintering was set at 700°C for 10 minutes. During sintering, the temperature was unstable and difficult to control. The potential was then reduced to 300W to try to stabilise the temperature. At the end the sample had melt in the centre and possibly boiled, resulting in the formation of dark glass bubbles in the centre of the material, as visible in Figure 40.

Table 14: Emissivity of the three simulants.

T (°C)	600	700	800	900	1000
e(LHS)	1.009	0.972	0.812	0.939	0.93
e(LMS)	1.012	0.972	0.831	0.945	0.941
e(MGS)	1.1	1	0.972	0.96	0.944
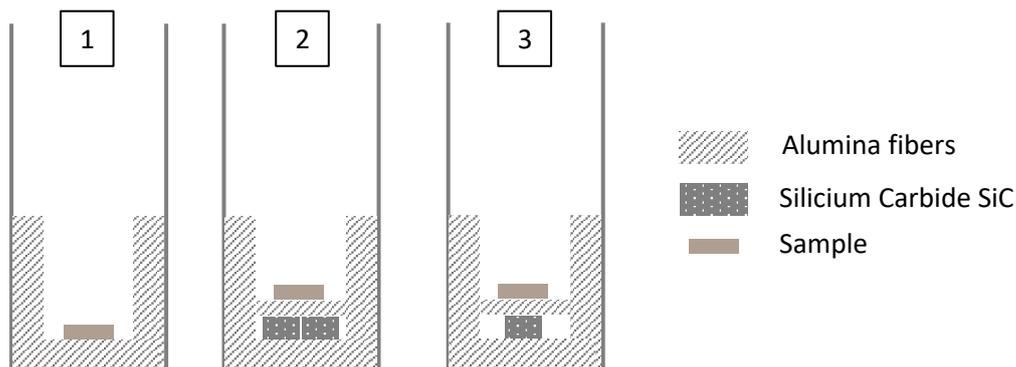
Figure 39: Schematics of the three combinations in quartz tube used for microwave sintering.

Figure 40: First LMS sample obtained with microwave sintering.

For the second attempt Carbide Silicium was added (Figure 39.2), the potential was divided by two, and the temperature remained stable during the process. The increase was far slower than for the first attempt, and no major problem occurred. The resulting sample is visible in Figure 41, and named as LMSm-2.5-MW700/10.

Figure 41: Second LMS sample obtained with microwave sintering.

LHS was used for the third attempt. The quantity of Silicium carbide was divided by two comparing to the previous try, and the setting was the same (Figure 39.3). A plasma formed at about 260°C, and so the process was stop. The sample shows a localised redd-ish colour while the rest of the sample kept

Potential (W)	270	360	450	540	630	720
Time (min)	5	5 ; 8 ; 10	3 ; 5 ; 10	5 ; 10 ; 15	5 ; 10 ; 15	3 ; 5 ; 10 ; 15 ; 20

the same colour than the green body, as visible in Figure 42. Plasma may have formed because of the metallic deposit remaining on the edge of the sample. This may have resulted in a localised heating visible as the red part.

Figure 42: LHS sample obtained with microwave sintering.

Many attempts were realised, with varying potential, time, temperature and sample arrangement, but the process was difficult to optimize. On one hand, microwave sintering is a relatively new process and is consequently not fully understand and mastered yet. On the other hand, LMS-1 and LHS-1 are recently developed simulants, meaning that few scientific literature on their processing, in particular on sintering, exists for the moment.

4.3.2.2. Multimodal microwave

A green body of unmilled LMS of around 2 cm diameter and less than 1 cm length was put in the oven under different potential and time. Table 15 gathers all potential/time combinations used. From 450 W and 5 min the sample began to heat significantly. However, a sintering and cohesive structure was never reached. Indeed, the sample remained friable, and break when a pressure was applied at the end. It also revealed that similar potential and similar or longer sintering time in monomodal and multimodal oven do not give the same results, and so probably not the same material behaviour.

Table 15: Combinations of parameters used for multimodal microwave sintering.

Although it is not a new technology, multimodal microwave sintering is also a relatively new way of processing, not perfectly known, and poorly studied with lunar simulants. Attempts realized in this project are part of a first approach to understand the behaviour of LMS simulant with this process.

4.4. FESEM

4.4.1. LHS

Figure 43 gathers FESEM images of LHS simulant before (Figure 43a) and after (Figure 43b) milling. The difference in grain size between the two images is clearly visible. Before milling, the wide granulometry is shown by the presence of big grains of about 100 µm, as well as small grains of a few tens of micrometres, and the average grain size measured is 42.23 ± 37.64 µm (Table 16). On the contrary, after milling no grains significantly bigger are visible on Figure 43b, and the average grain size became 4.16 ± 2.95 µm, with a reduced standard deviation too. Nevertheless, an agglomerate on the right side of Figure 43b seems to have formed, while none are visible on Figure 43a. This can be due to electrostatic forces produced during milling, which tend to gather particles, leading to the formation of agglomerates.
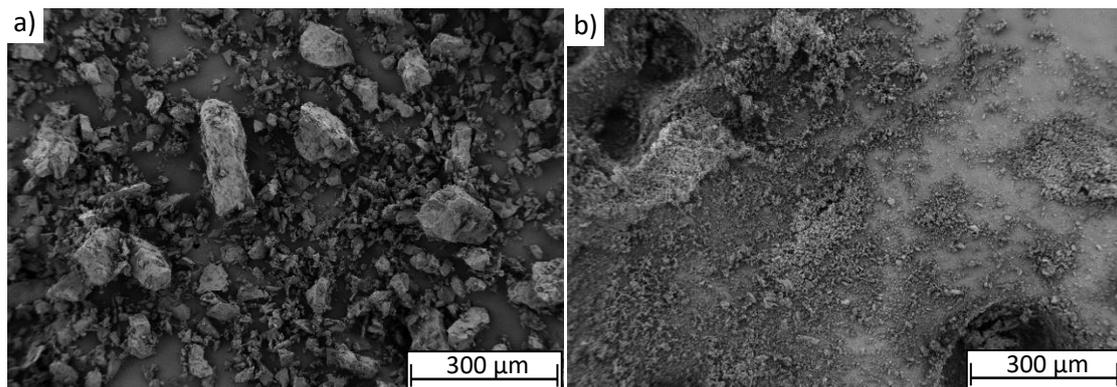
Figure 43: FESEM image of (a) raw LHS simulant and (b) milled LHS.

Table 16: Average grain size of LHS simulant before and after miling.

Material	Average grain size (µm)
Raw LHS	42.23 ± 37.64
Milled LHS	4.16 ± 2.95

Concerning sintered samples, FESEM image of LHSm-5-CS1000/1 is visible on Figure 44a, LHSm-2.5-CS1000/1 on Figure 44b, LHSm-2.5-CS1100/1 on Figure 43c, and LHSm-2.5-CS1100/2 on Figure 44d. As for LHS-2.5-CS1100/1, which FESEM image is visible on Figure 45.

A first noticeable thing is that all samples show an uneven surface, meaning that fracture didn't lead to grain fracture, but rather to their complete removal from the material. Furthermore, substantial open porosity is visible on all images, as well as globally poor bridge formation between grains. Some

are visible only for LHSm-5-CS1000/1 on Figure 44b, for LHSm-2.5-CS1100/1 on Figure 44c, and on Figure 45 for LHS-2.5-CS1100/1.
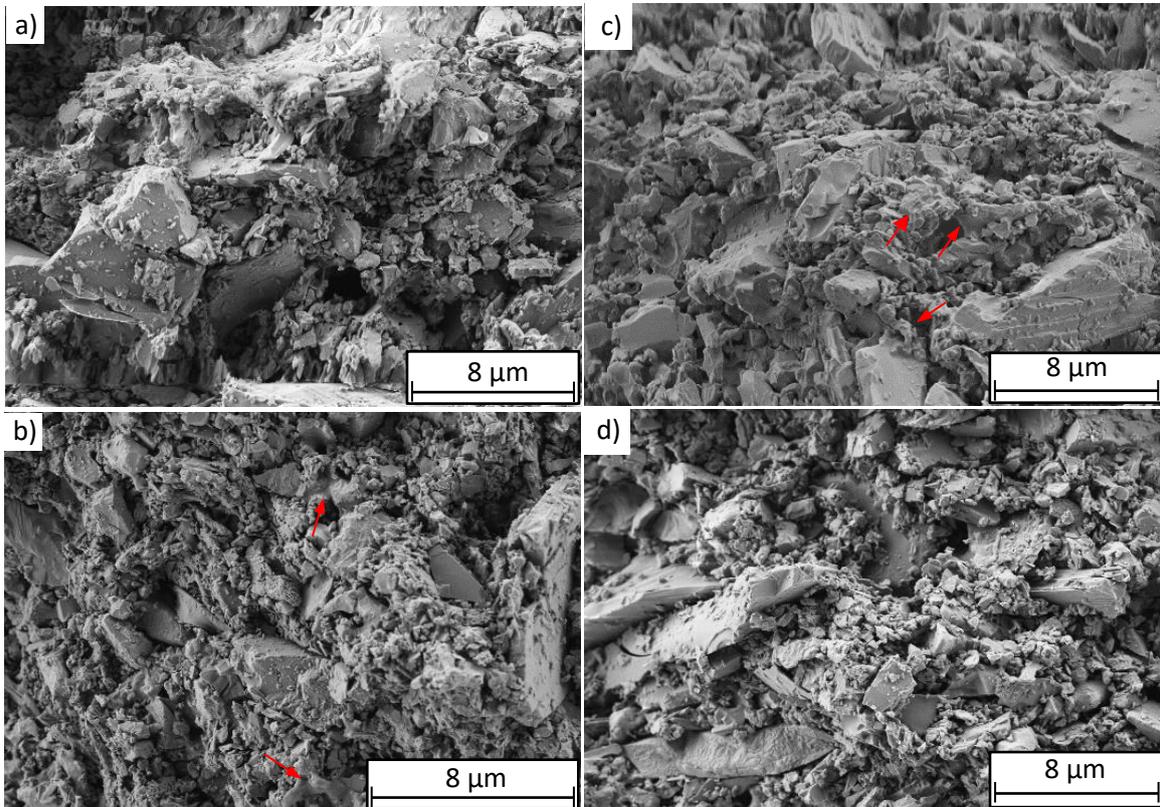
Figure 44: FESEM images a) LHSm-2.5-CS1000/1, b) LHSm-5-CS1000/1, c) LHSm-2.5-CS1100/1, and d) LHSm-2.5-CS1100/2.
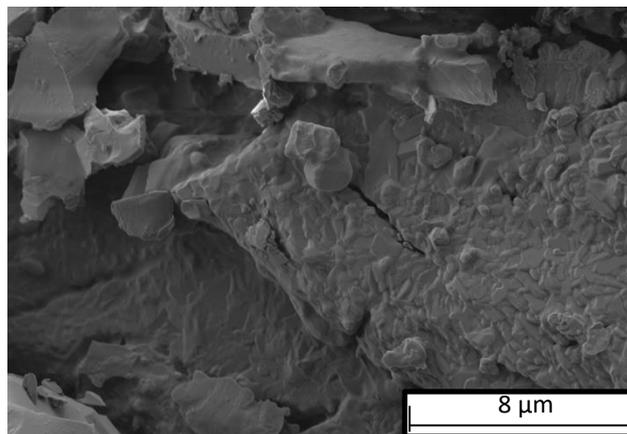
Figure 45: FESEM image of LHS-2.5-CS1100/1.

Finally, the average grain sizes measured in Table 17 are of the same order of magnitude than the grain sizes of milled and unmilled powder given in Table 16. This means that not grain growth occurred. This leads to the conclusion that these samples are not sintered enough, and that sintering 1100 °C for 1 h seems to allow the formation of the first bridges between grains.

Table 17: Average grain size of sintered LHS samples.

Material	Average grain size (μm)
LHSm-5-CS1000/1	1.07 ± 0.70
LHSm-2.5-CS1000/1	1.29 ± 1.72
LHSm-2.5-CS1100/1	1.60 ± 1.75
LHSm-2.5-CS1100/2	2.11 ± 1.48
LHS-2.5-CS1100/1	14.66 ± 17.93

4.4.2. LMS

Concerning LMS simulant before and after milling, FESEM images are visible on Figure 46a and b, respectively. Similarly to LHS simulant, the difference in granulometry and grain size is visible. Big grains and very small grains are visible in Figure 46a, with an average grain size and significant standard deviation of 45.75 ± 39.76 μm (Table 18). However, on Figure 46b, no significant bigger grains are visible, as traduced by the average grain size and reduced standard deviation of 9.51 ± 4.42 μm. And again, no agglomerates are visible with raw powder while some are visible on Figure 46b, confirming the hypothesis of electrostatic forces created during milling.
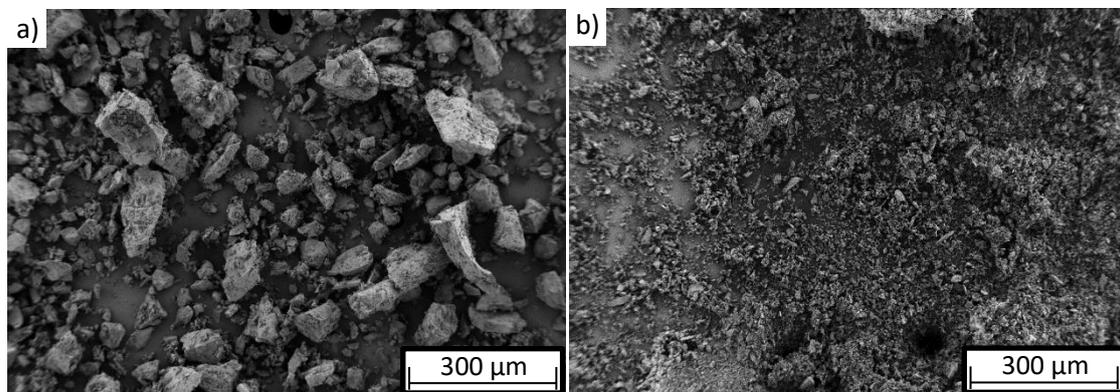

*Figure 46: FESEM image of (a) raw LMS simulant and (b) milled LMS.*

Table 18: Average grain size of LMS simulant before and after milling.

Material	Average grain size (μm)
Raw LMS	45.75 ± 39.76
Milled LMS	10.9 ± 5.23

Concerning sintered LMS samples, open porosity is also prevalent on all FESEM images (Figure 47a-b-c-d, Figure 48a-b, and Figure 49). An uneven surface is also visible on all FESEM images except Figure 47c, characteristic of grains removal during fracture. Figure 47c, corresponding to LMSm-2.5-

CS1100/1, shows a smoother surface that can be paralleled with its structure more sintered than all other LMS and LHS samples. Indeed, small grains are far less visible and large bridges are present between almost all grain. This structure appears more cohesive and may have led to grains fracture instead on grains removal, resulting in a smoother surface. However, its average grain size is 4.26 ± 1.34 µm (Table 19), and comparing to milled powder, which average grain size is 10.9 ± 5.23 µm, no grain growth seems to have happened.

Surprisingly, sintering LMS at 1100 °C for 2 hours leads to less bridges than for one hour, as shown by Figure 47d FESEM image of LMSm-2.5-CS1100/2. Finally, bridges are not visible on Figure 47a and b, FESEM images of LMSm-5-CS1000/1 and LMSm-2.5-CS1000/1, respectively.

Besides, sintering samples made with raw powder, corresponding to FESEM images 48a and b shows more bridges than LHS simulant. And microwave sintering of LMS at 700 °C for 10 minutes had not led to sintering, as no bridges are visible on Figure 49.
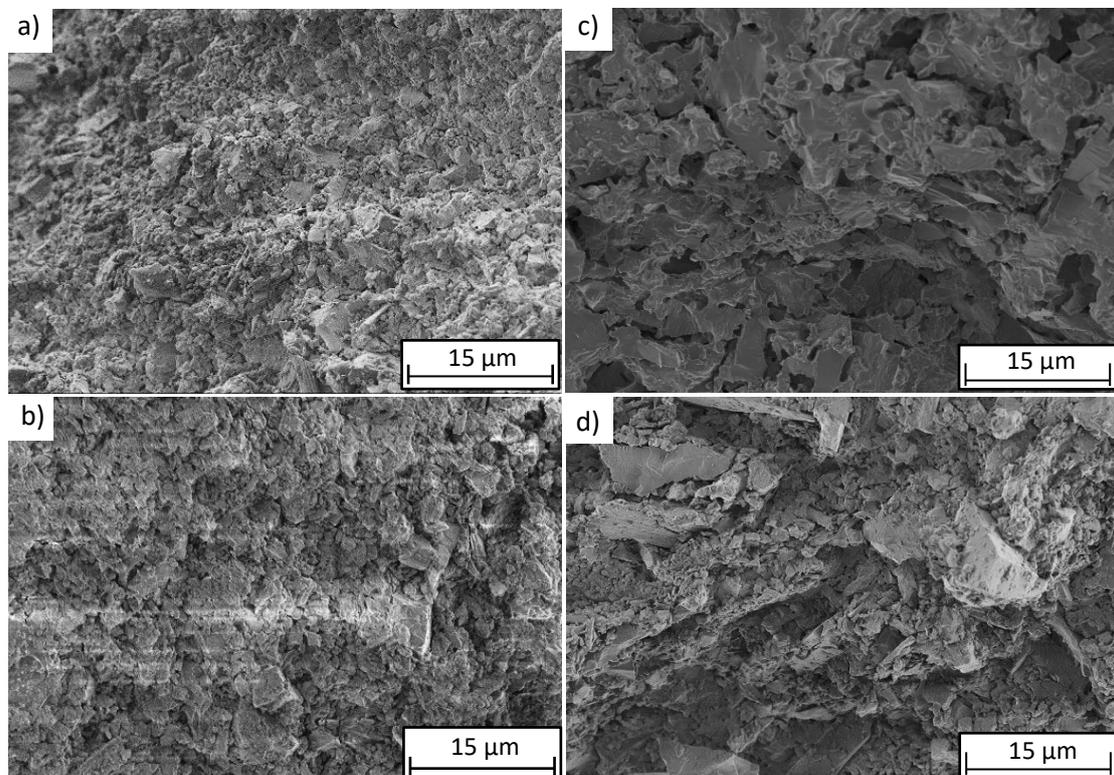
Figure 47: FESEM images of a) LMSm-2.5-CS1000/1, b) LMSm-5-CS1000/1, c) LMSm-2.5-CS1100/1, and d) LMSm-2.5-CS1100/2.
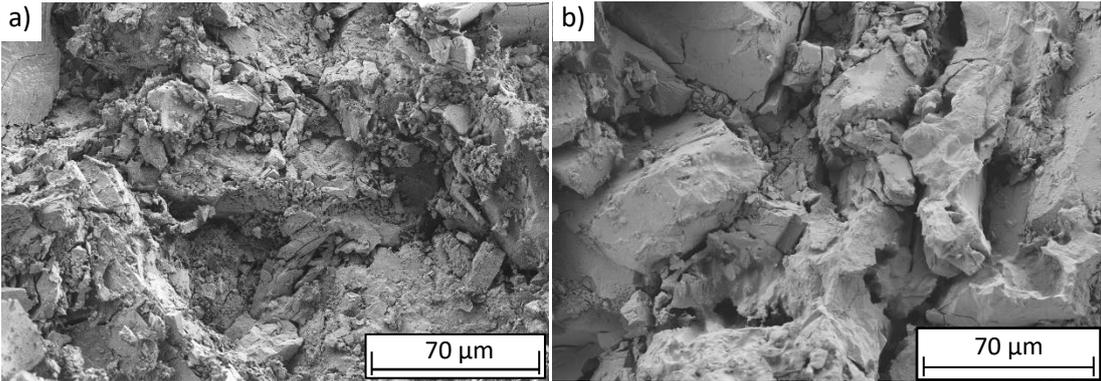
Figure 48: FESEM images of a) LMS-2.5-CS1000/1, and b) LMS-2.5-CS1100/1.
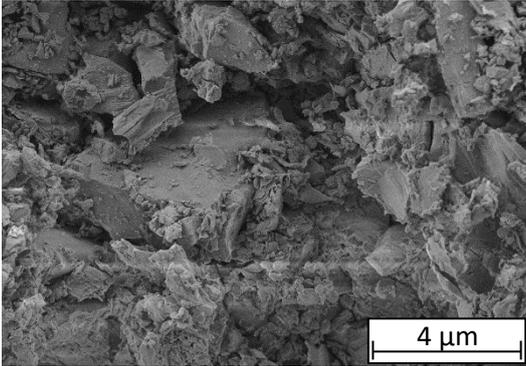
Figure 49: FESEM image of LMSm-2.5-MW700/10.

Table 19: Average grain size of sintered LMS samples.

Material	Average grain size (μm)
LMSm-5-CS1000/1	1.85 ± 1.06
LMSm-2.5-CS1000/1	0.76 ± 0.86
LMSm-2.5-CS1100/1	4.26 ± 1.34
LMSm-2.5-CS1100/2	2.65 ± 2.07
LMS-2.5-CS1000/1	13.49 ± 18.8
LMS-2.5-CS1100/1	16.21 ± 14.72
LMSm-2.5-MW700/10	3.09 ± 2.37

Consequently, even if the samples obtained after sintering LMS simulants are not consolidated, this material seems to sinter in conventional way more easily than LHS simulant. In the meantime, microwave sintering did not show any successful results.

4.4.3. MGS

Similarly to Moon simulants, unmilled MGS simulant (Figure 50a) shows big grains of more than 100 µm, as well as small grains of a few tens of micrometres. The average grain size and its consequent standard deviation is 24.48 ± 53.02 µm (Table 20). After milling the decrease of the average grain size is visible, as it became 9.51 ± 4.42 µm. Agglomerates are also visible in top of Figure 50b, because of the electrostatic forces due to milling.
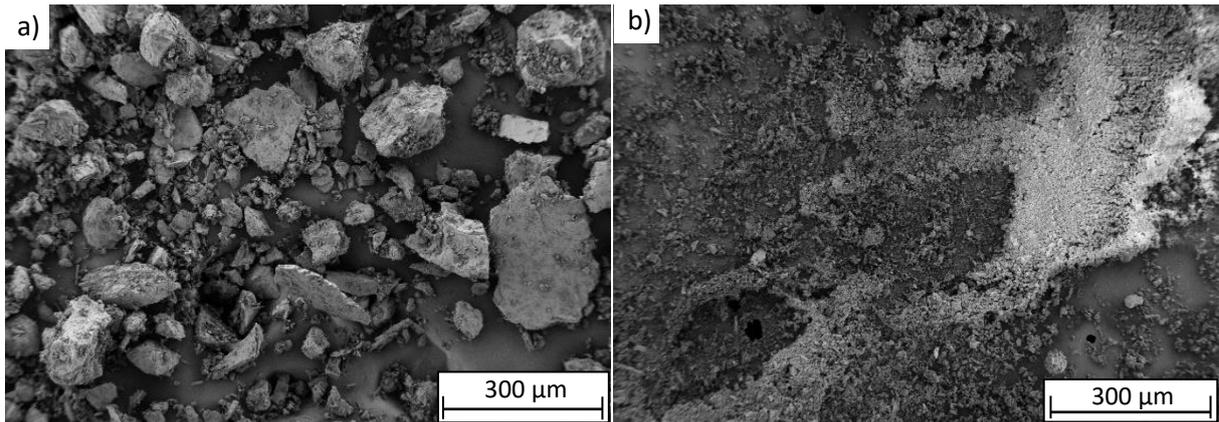
Figure 50: FESEM image of (a) raw MGS simulant and (b) milled MGS.

Table 20: Average grain size of MGS simulant before and after milling.

Material	Average grain size (µm)
Raw MGS	24.48 ± 53.02
Milled MGS	9.51 ± 4.42

Concerning sintered MGS. Bridges are clearly visible on Figure 51c, corresponding to MGSm-2.5-CS1100/1, and seem to have also formed in Figure 51a, FESEM image of MGSm-5-CS1000/1. Their average grain size of 2.39 ± 1.64 µm and 1.16 ± 1.01 µm (Table 21), respectively, do not show signs of grain growth.
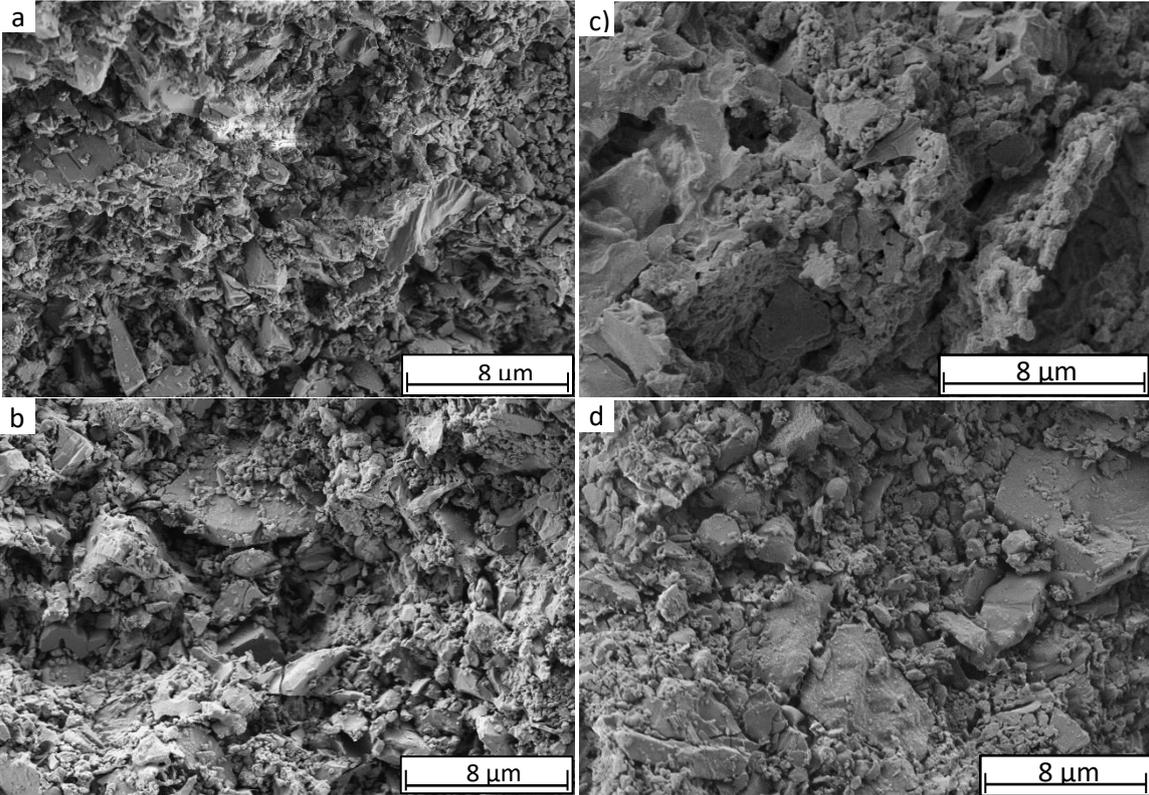
Figure 51: FESEM images of a) MGSm-2.5-CS1000/1, b) MGSm-5-CS1000/1, c) MGSm-2.5-CS1100/1, and d) MGSm-2.5-CS1100/2.
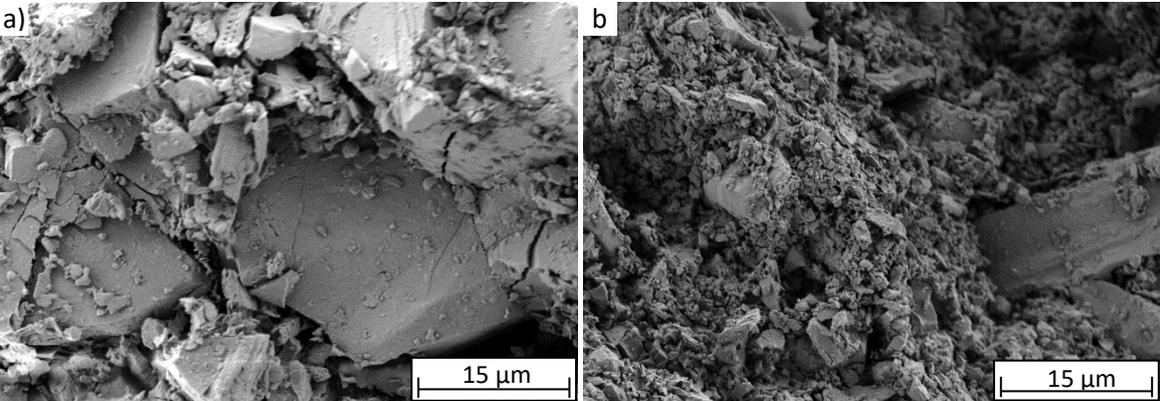
Figure 52: FESEM images of a) MGS-2.5-CS1000/1, and b) MGS-2.5-CS1100/1.

Table 21: Average grain size of sintered MGS samples.

Material	Average grain size (µm)
MGSm-5-CS1000/1	1.16 ± 1.01
MGSm-2.5-CS1000/1	1.23 ± 1.14
MGSm-2.5-CS1100/1	2.39 ± 1.64

MGSm-2.5-CS1100/2	2.28 ± 1.56
MGS-2.5-CS1000/1	11.33 ± 8.09
MGS-2.5-CS1100/1	2.23 ± 1.91

Otherwise, all others FESEM images, corresponding to MGSm-2.5-CS1000/1, MGSm-2.5-CS1100/2, MGS-2.5-CS1000/1, and MGS-2.5-CS1100/1, do not show bridge formation between grains. Furthermore, significant open porosity and uneven surfaces are also visible. Globally, MGS samples are not sufficiently sintered.

4.5. Density

Density was measured with Archimedes method, and values are visible in Table 22, 23 and 24, for LMS, LHS and MGS respectively and it is important to keep in mind that this technique only takes into account closed porosity.

Table 22: Density of LMS sintered samples.

Sample	Density (%)
LMS-2.5-CS700/1	98.19
LMS-2.5-CS900/1	98.74
LMS-2.5-CS1000/1	98.67
LMS-2.5-CS1100/1	96.63
LMSm-5-CS1000/1	93.89
LMSm-2.5-CS1000/1	94.47
LMSm-2.5-CS1100/1	96.28
LMSm-2.5-CS1100/2	94.78

Table 23: Density of LHS sintered samples.

Sample	Density (%)
LHS-2.5-CS700/1	99.69
LHS-2.5-CS900/1	98.50
LHS-2.5-CS1000/1	98.28
LHS-2.5-CS1100/1	97.70
LHS-2.5-CS1200/1	87.12
LHSm-5-CS1000/1	100
LHSm-2.5-CS1000/1	100
LHSm-2.5-CS1100/1	100
LHSm-2.5-CS1100/2	100

Concerning LMS samples with unmilled powder, the densities are between 96 % and 99 %, and there is no clear increase or decrease depending on the sintering temperature. Similarly, for LMS samples

with milled powder no clear influence of the sintering temperature is noticeable, with values between 93 and 97 %. Consequently, for this simulant, only the granulometry seems to have an effect on the density, as a lower density was globally obtained with a finer granulometry. For the LHS samples with unmilled powder, the density decreases from 99.56 % to 87.12 % with increasing sintering temperature. And for LHS samples with milled powder, the density reaches 100% and consequently have better density than unmilled powder samples.

Table 24: Density of MGS sintered samples.

Sample	Density (%)
MGS-2.5-CS700/1	100
MGS-2.5-CS900/1	100
MGS-2.5-CS1000/1	100
MGS-2.5-CS1100/1	99.16
MGSm-5-CS1000/1	100
MGSm-2.5-CS1000/1	100
MGSm-2.5-CS1100/1	100
MGSm-2.5-CS1100/2	100

For MGS samples the calculated density reaches 100 %, and 99.16 % for MGS-2.5-CS1100/1. Generally, the calculated densities are very high. On the other hand, FESEM images of all the sintered sample revealed a visible and significant open porosity. This contradiction demonstrates that Archimedes method is not suitable for a highly porous material, and consequently the densities previously calculated cannot be considered.

4.6.Microhardness
4.6.1. Lunar simulants

Figure 52 shows the microhardness of samples made of milled LHS and LMS and sintered in conventional method. The two materials show opposite behaviour. Indeed, for a dwell time of one hour, LHS samples hardness decreases from 0.755 GPa to 0.490 GPa when the compression force decreases and the sintering temperature increases. Then, hardness increases to reach its maximum, 0.770 GPa, when increasing the dwell time. And vice versa, LMS hardness increases from 0.488 GPa to 1.15 GPa, its maximum, when decreasing the compression force and increasing the sintering temperature, then decreases to 0.564G Pa when hold two hours at 1100 °C. Generally speaking, all hardness values are in the same range. Besides, no hardness values could have been obtained for sintered samples made of unmilled powder for the two lunar simulants, as they were too friable.
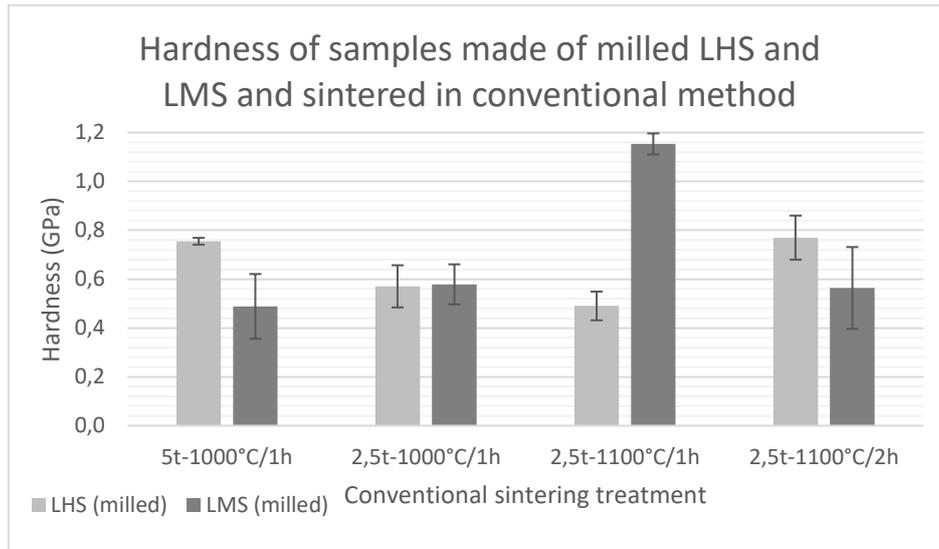
Figure 53: Hardness of LHS and LMS sintered samples.

By confronting FESEM images of LHS sintered samples (Figure 44) with hardness values in Figure 53, no clear influence is visible. Indeed, LHSm-5-CS1000/1 and LHSm-2.5-CS1100/1 both show some bridges, while they have the second highest hardness (0.76 GPa), and the smallest one (0.49 GPa), respectively, of LHS samples.

For LMS, the FESEM image with the most sintered structure (Figure 47c) correspond to LMS-2.5-CS1100/1, and has the highest hardness of all samples, being 1.15 GPa. In the meantime, LMS-2.5-CS1100/2 sample shows some bridges on Figure 47d, but has the lowest hardness value, 0.48 GPa.

Concerning LMS sintered in a monomodal microwave sintering oven, the hardness was measured at 0.51 ± 0.07 GPa. It is part of the lowest hardness value of LMS. This is consistent with Figure 49, its FESEM image, which does not show a sintered structure.

Consequently, except for LMSm-2.5-CS1100/1, all the samples did not reach a sufficient sintering stage during the process to have a significant influence on the hardness. Only LMSm-2.5-CS1100/1 showed a more advanced sintered structure, and therefore has the highest hardness.

4.6.2. Mars simulant

Concerning MGS samples, hardness decreases from 0.68 GPa to 0.43 GPa when decreasing the compression of the powder. Then, it increases until 0.99 GPa when sintering temperature and sintering time increase. Only MGSm-2.5-CS1100/1 show bridges on its FESEM image (Figure 51c), and has a hardness of 0.69GPa, the second highest value on Figure 54. Again, all measured hardness values are in the same range.
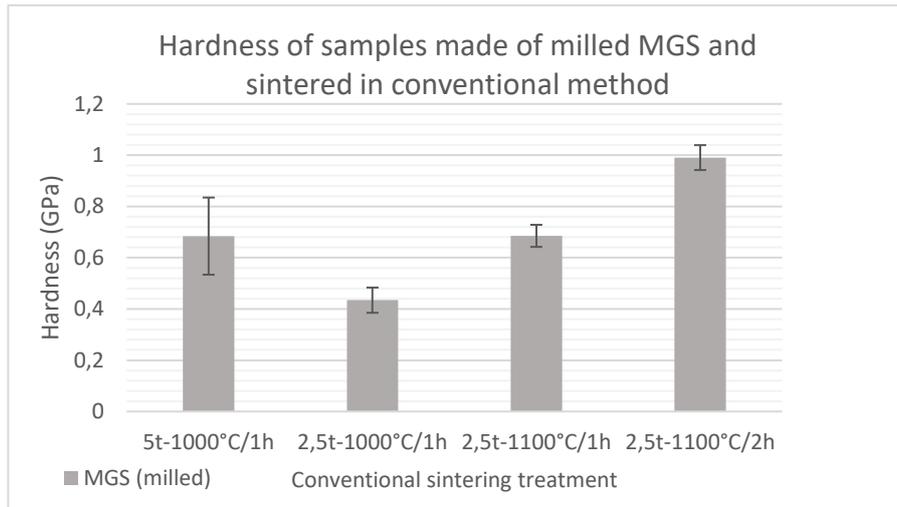
Figure 54: Hardness of MGS sintered samples.

So, as for lunar simulant, FESEM images of MGS samples do not show a sufficient sintering stage to determine an influence of it on the hardness.

5. Conclusion

The accomplishment of this Master's Thesis led to the following conclusions:

- Lunar simulants LHS-1 and LMS-1, as well as Mars simulant MGS-1 have been studied in conventional and microwave sintering.

- Milling led a significant reduction of grain size and to the apparition of agglomerates in the powders, probably due to electrostatic forces. Green bodies made of raw simulants resulted less fragile but more friable at the surface than green bodies made of milled simulants. After conventional sintering, LHS and LMS samples showed a beginning of sintering in samples made of raw and milled simulant, while MGS samples showed sintered structure only with milled powder.

- Compaction at 2.5 t and 5 t gave opposite hardness behaviours with the two lunar simulants. Concerning MGS simulant, compacting under higher pressure seems to lead to higher hardness.

- Globally, conventional sintering led to uncomplete sintered samples, which explains hardness values being in the same range but showing different behaviours depending on the material. However, LMSm-2.5-CS1100/1 showed the most sintered structure and had the highest hardness, which is consistent. Longer sintering time may give more sintered structure.

- Attempts in microwave sintering are one of the first realised with these simulants. Several attempts were realised with monomodal microwave with varying potential and cavity arrangement. Optimal parameters revealed to be difficult to find, and side reactions (melting, plasma) occurred. The same parameters used in multimodal microwave oven gave different results for the same material, and seemed less efficient. Tests should be pursued jointly with progress realised in this process.

To go further, sintering in vacuum would be interesting to better represent space conditions, and compression and impact tests would complete mechanical properties characterization. The study of samples aging could also help predict potential problems linked to extreme temperature cycles or radiation.

6. Budget
6.1. Estimation of costs
6.1.1. Equipment

All the machines used for this project are gathered in Table 25 with their price. They all remain in the laboratory and most of them are used for several years, meaning that some machines are now amortized. Despite that, they represent an initial investment of 211 845€. Furthermore, small equipment that is necessary to prepare samples is listed in Table 26.

Table 25: Price of laboratory equipment.

Equipment	Quantity	Unit price (€)
Cutting machine with cutting disk Stamping machine Polishing machine with discs	1	63000
Drying stove	1	2350
Planetary ball mill	1	15000
Laser Particle Size Analyzer	1	32000
Uniaxial press	1	8000
Conventional oven		28000
Monomodal microwave oven	1	50000
Multimodal microwave oven	1	170
Portative durometer	1	5000
Heating plate	1	325
Precision balance and density measurement equipment	1	8000
Total		211845

Table 26: Price of laboratory small equipment.

Small equipment	Quantity	Unit price (€)	Cost (€)
Sieve	1	120	120
Porcelain evaporator	6	30	180
Polishing discs	7	200	1400
Spatula	1	2.89	2.89
Pliers	1	2.55	2.55
Beakers	6	5	30
Quartz tube	1	30	30
Total			1760

6.1.2. Energy

Table 27: Estimation of energy consumption.

Equipment	Power (W)	Time of use (hour)	Quantity (Wh)
Cutting machine	750	4	3000
Stamping machine	1000	3.25	3250
Polishing machine	570	8.17	4655
Drying stove	1600	24	38400
Planetary ball mill	1200	8	9600
Conventional oven	4500	10	45000
Monomodal microwave oven	700	1	700
Multimodal microwave oven	900	2.7	2430
Heating plate	1020	21	21420
Precision balance	15.5	2	31
Total			128486

Table 28: Estimation of energy cost.

Energy unit	Quantity	Unit price (€)	Total energy cost (€)
kWh	128.486	0.103	13.23

6.1.3. Characterization costs

Table 29: Characterization cost.

Technique	Time (h)	Price per hour (€/h)	Characterization cost (€)
FESEM	10	20	200

6.1.4. Material costs

Table 30: Material cost.

Material	Quantity (kg)	Price per kg (€/kg)	Material cost (€)
LHS-1	0.04	35	1.4
LMS-1	0.04	35	1.4
MGS-1	0.034	35	1.19
Total			3.99

6.1.5. Labor costs

Table 31: Labor cost.

	Time (h)	Price per hour (€/h)	Labor cost (€)
Project directors	100	50	5000
Student engineer	250	25	6250
Total			11250

6.2.Total of the costs

Table 32: Total of costs.

Category	Cost (€)
Small equipment	1760
Energy	13.23
Characterization	200
Material	3.99
Labor	11250
TOTAL	**13 227.22**

The total cost for the realisation of this project is estimated at 13 227.22 €.

7. References

M. Abd Mutalib, M.A. Rahman, M.H.D. Othman, A.F. Ismail, J. Jaafar (2017). *Scanning Electron Microscopy (SEM) and Energy-Dispersive X-Ray (EDX) Spectroscopy.* Membrane Characterization, Chapter 9. doi:10.1016/B978-0-444-63776-5.00009-7.

D. Bernache-Assolant, J-P. Bonnet. *Frittage: aspects physico-chimiques – Partie 1: frittage en phase solide*. Techniques de l'Ingénieur (2005), ref. AF6620 V1.

D. Bernache-Assolant, J-P. Bonnet. *Frittage: aspects physico-chimiques – Partie 2: frittage en phase liquide*. Techniques de l'Ingénieur (2005), ref. AF6621 V1

Borrell Tomás, Mª Amparo; Salvador Moya, Mª Dolores. *Materials cerámicos avanzados: procesado y aplicaciones.* Valencia: Editorial Universitat Politècnica de València (2018).

Kevin M. Cannon, Daniel T .Britt, Trent M. Smith, Ralph F. Fritsche, Daniel Batcheldor. *Mars Global Simulant MGS-1: A Rocknest-based open standard for basaltic martian regolith simulants.* Icarus, Volume 317 (2019). https://doi.org/10.1016/j.icarus.2018.08.019.

Caruso, John & Spina, D. & Greer, Lawrence & John, Wentworth & Michele, Clem & Krasowski, Mike & Prokop, Norman. *Excavation on the Moon: Regolith Collection for Oxygen Production and Outpost Site Preparation* (2008). DOI: 10.2514/6.2008-808.

Giacomo Certini, Suniti Karunatillake, Yu-Yan Sara Zhao, Pierre-Yves Meslin, Agnes Cousin, Donald R. Hood, Riccardo Scalenghe. *Disambiguating the soils of Mars*. Planetary and Space Science, Volume 186 (2020). https://doi.org/10.1016/j.pss.2020.104922.

Exolith Lab. *Simulant Introduction* [online]. Disponible sur : https://exolithsimulants.com/pages/simulant-introduction/ [visited in December 2021].

Kevin W. Farries, Phillip Visintin, Scott T. Smith, Philip van Eyk. *Sintered or melted regolith for lunar construction: state-of-the-art review and future research directions*. Construction and Building Materials, Volume 296 (2021). https://doi.org/10.1016/j.conbuildmat.2021.123627.

Lawrence A. Taylor, Thomas T. Meek. *Microwave sintering of Lunar Soil: Properties, Theory, and Practice*. Journal of Aerospace Engineering, Volume 18, Issue 3 (2005). https://doi.org/10.1061/(ASCE)0893-1321(2005)18:3(188).

Shannon L. Taylor, Adam E. Jakus, Katie D. Koube, Amaka J. Ibeh, Nicholas R. Geisendorfer, Ramille N. Shah, David C. Dunand. *Sintering of micro-trusses created by extrusion-3D-printing of lunar regolith inks*. Acta Astronautica, Volume 143 (2018). https://doi.org/10.1016/j.actaastro.2017.11.005.

D. Karl, K.M. Cannon, A. Gurlo. *Review of space resources processing for Mars missions: Martian simulants, regolith bonding concepts and additive manufacturing*. Open Ceramics (2022). doi: https://doi.org/10.1016/j.oceram.2021.100216.

David Karl, Franz Kamutzki, Pedro Lima, Albert Gili, Thomas Duminy, Andrea Zocca, Jens Günster, Aleksander Gurlo. *Sintering of ceramics for clay in situ resource utilization on Mars*. Open Ceramics, Volume 3 (2020). https://doi.org/10.1016/j.oceram.2020.100008.

David S. McKay, Grant Heiken, Abhijit Basu, George Blanford, Steven Simon, Robert Reedy, Bevan M. French, and James Papike. *The Lunar Regolith*. Lunar sourcebook, Chapter 7, Cambridge University Press (1991).

E. N. Slyuta. *Physical and mechanical properties of the lunar soil (a review)*. Solar System Research, Volume 48, No. 5 (2014). DOI: 10.1134/S0038094614050050.